Surfaces and Interfaces 44 (2024) 103779

Contents lists available at ScienceDirect

Surfaces and Interfaces

journal homepage: www.sciencedirect.com/journal/surfaces-and-interfaces

Synthesis and characterisation of magnesium-wrapped hydroxyapatite nanomaterials for biomedical applications

Saleth Sebastiammal [a,*], Arul Sigamani Lesly Fathima [a], Khalid A. Al-Ghanim [b], Marcello Nicoletti [c], Gurunathan Baskar [d,e], Jayaraj Iyyappan [f], Marimuthu Govindarajan [g,h,*]

[a] Research Department of Physics, Holy Cross College (Autonomous), Nagercoil 629004, Tamil Nadu, India
[b] Department of Zoology, College of Science, King Saud University, Riyadh 11451, Saudi Arabia
[c] Department of Environmental Biology, Sapienza University of Rome, Rome 00185, Italy
[d] Department of Biotechnology, St. Joseph's College of Engineering, Chennai, India
[e] School of Engineering, Lebanese American University, Byblos, Lebanon 1102 2801
[f] Department of Biotechnology, Saveetha School of Engineering, Saveetha Institute of Medical and Technical Sciences (SIMATS), Thandalam, Chennai 602107, India
[g] Unit of Vector Control, Phytochemistry and Nanotechnology, Department of Zoology, Annamalai University, Annamalainagar 608 002, Tamil Nadu, India
[h] Department of Zoology, Government College for Women (Autonomous), Kumbakonam 612 001, Tamil Nadu, India

ARTICLE INFO

Keywords:
Magnesium doped hydroxyapatite
Curcumin
Anticancer activity
Antimicrobial activity

ABSTRACT

The advancement of novel nanobiomaterials holds significant importance in the fields of drug delivery and environmental remediation. Hydroxyapatite, which falls under the category of bioceramic materials, has demonstrated efficacy as a bone graft material. The substitution of cations in hydroxyapatite has been found to enhance its biological properties, making it a promising material for various biomedical applications. In this study, the synthesis of Mg^{2+} substituted hydroxyapatite nanostructures was conducted through the sol-gel method employing different surfactants, namely polyethylene glycol and cetyltrimethylammonium bromide. The resulting nanoparticles were subjected to analysis to evaluate their structural, morphological, and optical characteristics. The antimicrobial and antioxidant behavior of the Mg^{2+} doped hydroxyapatite nanoparticles were also studied. The XRD analysis showed a hexagonal crystal structure for Mg^{2+} doped hydroxyapatite nanostructures for all samples. The Raman and FTIR results also confirmed the successful substitution of divalent cation Mg^{2+} in hydroxyapatite. EDAX results exhibited the qualitative elemental composition and stoichiometric nature of synthesized hydroxyapatite. The optical study showed higher transmission in the visible region for the Mg^{2+} doped hydroxyapatite prepared using various surfactants. The microbial restriction efficacy of Mg^{2+} doped hydroxyapatite prepared using various surfactants was examined against human pathogenic bacterias *Shigella flexneri* (MTCC-2197), *Escherichia coli* (MTCC-4213), *Pseudomonas aeruginosa* (MTCC-3131), *Klebseilla pneumoniae* (MTCC-1214), and *Staphylococcus aureus* (MTCC-3123). The hydroxyapatite nano biomaterial doped with Mg^{2+} demonstrates remarkable antibacterial, antifungal, and antioxidant properties. The HeLa cell lines exhibited significant cytotoxicity when exposed to magnesium ion-doped hydroxyapatite nanoparticles.

1. Introduction

Nanotechnology presents vast potential in revolutionizing biomedical applications due to its minute scale and diverse capabilities. At the nanoscale, materials exhibit unique properties that can be tailored for targeted drug delivery systems. Nanoparticles offer precise control in releasing medications, enhancing treatment efficacy and minimizing side effects. Nano-based imaging tools enable highly sensitive diagnostics for early disease detection, fostering improved healthcare outcomes. The development of nanobiosensors facilitates real-time monitoring of biomarkers, aiding in disease management and personalized medicine. Nanomaterials serve as scaffolds for tissue engineering,

Abbreviations: CTAB, cetyltrimethylammonium bromide; EDAX, Energy-dispersive X-ray analysis; EDTA, ethylene diammine tetra acetic acid; FESEM, field emission scanning electron microscopy; FTIR, Fourier transform infrared spectroscopy; HAp, Hydroxyapatite; Mg, Magnesium; MTCC, Microbial Type Culture Collection; MTT, 3-(4, 5-dimethylthiazolyl-2)−2, 5-diphenyltetrazolium bromide; NPs, nanoparticles; PEG, polyethylene glycol; XRD, X-ray diffraction.

* Corresponding authors.
E-mail addresses: sebastiammal.s@holycrossngl.edu.in (S. Sebastiammal), drgovind1979@gmail.com (M. Govindarajan).

https://doi.org/10.1016/j.surfin.2023.103779
Received 6 August 2023; Received in revised form 8 December 2023; Accepted 16 December 2023
Available online 19 December 2023

fostering regenerative therapies for damaged tissues or organs. Nanostructured coatings on medical devices prevent infections and improve biocompatibility, enhancing their functionality. The versatility of nanotechnology allows for the creation of advanced biomaterials with improved mechanical and biological properties. Research in nanomedicine continues to explore novel applications, holding promise for groundbreaking solutions in healthcare. The integration of nanotechnology in biomedical realms holds the potential to revolutionize diagnosis, treatment, and overall patient care [22,23,27,51].

Nanoscale biomaterial is the topic of interest in the latest biomedical research in which bioceramic material was explored for biomedical applications due to their unique physical, mechanical and biological properties [46]. In the last fifty years, there has been a revolution in the use of bioceramics to improve human well-being. Hydroxyapatite (HAp) based bioceramic materials have excellent biocompatibility and osteoconductivity. HAp nanoparticles have suitable stoichiometry with human bones [1]; hence, they can be used for bone implantation and regeneration [2]. Crystallinity and crystal size are two parameters that determine the solubility of HAp for biological applications. However, the capacity to generate new bone tissue is limited [42], and HAp has poor mechanical strength in wet conditions [30]. This phenomenon can be controlled or improved by incorporating foreign elements in HAp [46]. Hence, analysing the ionic substitution in the HAp lattice is necessary for effective usage in biological applications.

Cations such as Sr^{2+}, Ag^{+}, Zn^{2+}, Mg^{2+}, Ce^{3+}, Gd^{3+}, Y^{3+}, and La^{3+} can be substituted into the hydroxyapatite lattice to improve their properties [14,24,43]. Among the various cations, Mg^{2+} incorporated HAp is expected to show excellent biological properties [48]. Bone fragility is decreased because of Mg^{2+}'s indirect effect on mineral metabolism. Moreover, Mg^{2+} reduces human exposure to potential osteoporosis risk factors [31]. Mg^{2+} speeds up the development of new blood vessels by stimulating the endothelium to produce nitric oxide and migrate and expand [11]. Bone mineral density drops in rats fed Mg-deficient diets, whereas greater levels of this mineral were linked to healthier bones [11]. Furthermore, the utilization of specific substitutional components in an individual's skeletal structure is influenced by various factors, including dietary habits, age, and gender [15].

Using the precipitation technique, Nagyné-Kovács et al. [37] reported that Mg-substituted HAp samples with 2 and 4 mol% of Mg/(Ca + Mg). The crystal size and lattice properties were both lowered by Mg insertion as the Mg level rose. In addition, it was observed that the inclusion of Mg-HAp strains exhibited a more pronounced inhibitory impact on both Gram-negative and Gram-positive bacteria than pure HAp strains [37]. According to another study, it was observed that subjecting human bone to incineration at a temperature of 900 °C resulted in an augmentation of crystal dimensions by several microns, accompanied by alterations in their morphology [33]. As a result, the annealing process confounds any attempt at objectively assessing the impact of the Mg addition. Importantly, the antimicrobial and antioxidant properties of Mg-doped HAp nanoparticles have received little attention. The current research focuses on the possible antimicrobial and antioxidant properties of Mg-doped HAp nanoparticles.

There are several methods employed in the production of monovalent and divalent doped hydroxyapatite (HAp), including microwave hydrothermal synthesis, co-precipitation, sol-gel method, solid-state reaction, and reversed microemulsion technique [46]. The Mg^{2+} doped HAp nanoparticles' morphology can be controlled using the low-cost, simple sol-gel approach. The selection of an appropriate stabilizing agent is paramount in synthesizing magnesium-doped hydroxyapatite (HAp). The different stabilizing agent has different effect on the Mg^{2+} doped HAp and should not have a toxic effect. The stabilizers such as ethylene diammine tetra acetic acid (EDTA), cetyltrimethylammonium bromide (CTAB), carboxy methyl cellulose and polyethylene glycol (PEG 400) were used for the preparation of Mg^{2+} doped HAp [49]. Recently, the utilization of green stabilizers has gained much importance due to their eco-friendly nature, higher biodegradability, and lower toxicity [7]. The utilization of extract derived from medicinal herbs with a long-standing history of traditional use can be employed as a stabilizing agent in the production of nanoparticles [5]. Utilizing these botanical specimens can potentially enhance the biological characteristics of the magnesium-doped hydroxyapatite nanoparticles [25]. This motivates us to study the effect of chemical and green stabilizers of Mg^{2+} doped HAp nanoparticles.

Curcumin is a polyphenolic chemical derived from the rhizome of *Curcuma longa*. Curcumin has diverse effects including the ability to promote wound healing, as well as possessing antibacterial, antioxidant, and anti-inflammatory activities. Additionally, it has anti-cancer capabilities [45]. Nevertheless, the pharmaceutical and food sectors encounter challenges in harnessing the potential of curcumin owing to its volatility, prominent hydrophobic characteristics, and restricted capacity to be absorbed orally [44]. Tackling these problems is a pressing need in order to fully harness the promise of curcumin in many applications.

In this present study, an attempt was made to synthesize divalent cation (Mg^{2+}) doped HAp nanoparticles with or without chemical surfactants (PEG/CTAB) and with green capping agent (curcumin extract) through sol-gel technique and to study its antimicrobial, antioxidant, anticancer and toxicity properties.

2. Materials and methods

2.1. Materials

All of the chemicals used were of analytical quality and were acquired from SRL chemicals in India. These included di-ammonium hydrogen phosphate ($(NH_4)_2HPO_4$), calcium nitrate ($Ca(NO_3)_2{\cdot}4H_2O$), CTAB, PEG 400, and ammonia. Curcumin (Art No.820354) was obtained from Merck, India. During all of the experiments, double-distilled water was used as the solvent.

2.2. Preparation of divalent (Mg^{2+}) doped hydroxyapatite NPs

The synthesis procedure was conducted in accordance with the methodology outlined by Sebastiammal et al. [46], with slight adjustments made. Separately, 50 mL of deionized water was combined with about 0.9 M of calcium nitrate and 0.1 M of cationic solution containing magnesium nitrate [48], and the mixtures were agitated using a magnetic stirrer for 30 min. Additionally, a solution containing approximately 0.6 M of di-ammonium hydrogen phosphate was combined with the previously prepared solution. Later, dropwise addition of ammonia was included until it reached pH 10. The acquired reaction mixture was allowed to dry in a hot air oven and calcined at 500 °C for 2 h. Thus, prepared dried cake was powdered to obtain Mg^{2+}doped Hydroxyapatite (Mg^{2+}-HAp). To prepare Mg^{2+} doped HAp-PEG, Mg^{2+} doped HAp-CTAB and Mg^{2+} doped HAp curcumin extract, about 0.1 M of CTAB or PEG was dissolved in deionized water and curcumin extract (50 mL) was included with 0.9 M of calcium and 0.1 M of cationic solution magnesium solution. Later, the consecutive procedures were performed as Mg^{2+} doped hydroxyapatite was prepared to obtain prepared NPs.

2.3. Characterizations of Mg^{2+}doped HAp NPs

The crystallographic structural analysis was performed utilizing an XPERT-PRO powder diffractometer and monochromatic CuK (λ =1.5406) radiation, covering the 2θ range from 20° to 80° Additionally, a Fourier transform infrared (FTIR) spectrometer (Make: Bruker IFS48) analyzed the functional groups present in the synthesized compounds. The morphology and size of Mg^{2+}doped HAp NPs were investigated by a QUANTA 250 FEG field emission scanning electron microscopy (FESEM). Energy-dispersive X-ray spectroscopy (EDAX) was used to analyze the elemental components. Further, the Transmission Electron Microscope (TEM) Model JOEL, No. 1200 EX was employed to analyze

the microstructure of the synthesized compound. Subsequently, a UV and photoluminescence spectrophotometer was employed to investigate the optical and photoluminescence characteristics.

2.4. Toxicity assay of Mg^{2+}doped HAp NPs

Toxicity assay of the different Mg^{2+} doped HAp samples from specific compounds was performed using the well diffusion method and the toxic substances were tested. The mineral salt medium was prepared with 15 % NaCl and sterilized. The Mg^{2+} doped HAp samples were placed on the surface of the agar plate using aseptic cotton swabs. The Mg^{2+} doped HAp NPs antibiotic disc was placed above the surface and incubated at 37 °C for 24 h. The plates were observed after incubation and the results were analyzed.

2.5. Antimicrobial activity of synthesized Mg^{2+}doped HAp NPs

Antibacterial activity of Mg^{2+} doped HAp NPs were assessed using the agar-well diffusion technique [38,40] against *Escherichia coli* (MTCC-4213), *Shigella flexneri* (MTCC-2197), *Pseudomonas aeruginosa* (MTCC-3131), *Klebseilla pneumoniae* (MTCC-1214) and *Staphylococcus aureus* (MTCC-3123). Initially, the prepared mueller hinton agar plates were inoculated with 100 μL of 10^6 CFU suspension of bacterial species. Later, aseptically wells with uniform diameter were created and about 50 μL of 40 mg/mL of synthesized Mg^{2+} doped HAp NPs were poured into these wells. After incubation at 37 °C for 24 h, the zone of inhibition was determined and subsequently expressed as the average values. The same methodology was employed to assess the antifungal activity against *Aspergillus niger, Odium caricae* and *Aspergillus flavus* with about 10^5 spores / mL was used as inoculum and the incubation period was 94 h [13,53].

2.6. Antioxidant activity of synthesized Mg^{2+}doped HAp NPs

The DPPH (2, 2-diphenyl-2-picrylhydrazyl hydrate) assay was employed with slight modifications to evaluate the antioxidant or scavenging activity of the synthesized Mg^{2+}-doped hydroxyapatite nanoparticles (HAp NPs) [4]. Here, 3.96 mg of DPPH was dissolved in 20 mL of methanol and 2.05 mL of DPPH solution was mixed with 1 mL of the sample solution. Rutin was explored as a standard. The absorbance at a wavelength of 517 nm was determined using UV–visible spectroscopy. The following Eq. (1) was used to determine the scavenging activity [13,53].

$$\text{DPPH scavenging activity (\%)} = \text{Abs (control)} - \text{Abs (sample)/Abs (control)} \times 100 \quad (1)$$

2.7. Cytotoxic activity of synthesized Mg^{2+}doped HAp NPs

MTT (3-(4, 5-dimethylthiazolyl-2)−2, 5-diphenyltetrazolium bromide) cell viability assay was performed to determine the anti-proliferation activity of synthesized Mg^{2+}doped HAp NPs against HeLa cell line [8]. The particular cell line was acquired from the National Centre for Cell Sciences (NCCS), Pune, India. Sub-culturing was performed using DMEM high glucose media. The cell density was maintained at a level of 20,000 cells per well. The negative control consisted of tumor cells and tumor cells without the test drug. The cancer cells were subjected to a concentration of 12.5 μg/mL of a standard drug, serving as a positive control. Various concentrations of Mg^{2+}doped HAp NPs (ranging from 6.25 to 100 μg) were dispensed into individual wells. After a 24-hour incubation period at a temperature of 37 °C, the cells' viability was evaluated by directly observing their vitality using an inverted phase-contrast microscope.

2.8. Analytical statistics

The examination of size variations within FESEM images of pure Mg^{2+} doped HAp, Mg^{2+} doped HAp-PEG, Mg^{2+} doped HAp-CTAB, and Mg^{2+} doped HAp-extract involved the use of the Student's *t*-test. Analysis was conducted using the statistical software Minitab 14.

3. Results and discussion

3.1. XRD analysis

The X-ray diffraction (XRD) technique was employed to analyze the crystalline structure of hydroxyapatite nanoparticles (HAp NPs) doped with magnesium ions (Mg^{2+}). Fig. 1 (a-d) displays the X-ray diffraction (XRD) pattern of hydroxyapatite nanoparticles (HAp NPs) doped with divalent magnesium ions (Mg^{2+}), both with and without the presence of surfactants. Fig. 1(a) represents the hexagonal HAp crystallization into a phase with diffraction peaks of Mg^{2+}doped HAp that follows the typical HAp pattern (JCPDS: 09–0432). The significant diffraction peaks observed at $2\theta = 25.89, 28.05, 31.15, 32.89, 34.62, 35.68, 42.03, 44.90, 47.28, 48.24, 53.39$ and 59.96 are assigned to (002), (102), (211), (300), (202), (301), (311), (400), (312), (320), (004) and (420) planes, respectively. The observed planes align with the anticipated arrangement of HAp, which is characterized by a hexagonal structure and is classified under the P63/m space group (JCPDS No: 09–0432). No additional impurity peaks were detected, suggesting that the Mg^{2+} doped HAp is in a single phase under the current experimental parameters. Magnesium and other contaminants have no secondary phase, which demonstrates that without altering HAp's crystal structure, magnesium ions have effectively replaced calcium ions. This finding is in strong agreement with the earlier study of Hongquan et al., [17]. Nevertheless, when some Ca^{2+} sites were replaced by Mg^{2+}ions, lattice cell characteristics showed deformation and a minor shift in 2 θ, which indicates that the dopant was significantly incorporated into the HAp lattice. The observed diffraction peaks for Mg^{2+}doped HAp are sharp and well-resolved, indicating that the synthesized Mg^{2+}doped HAp is well crystallized. Some peak reflections show a slight shift compared with pure HAp (JCPDS: 09–0432) and it might be due to changes in lattice parameters caused by the decreased ionic radius of Mg^{2+} (0.72 Å) replacing Ca^{2+} (0.99 Å) or may be due to the residual stress and defect. A similar outcome demonstrating the ionic alterations in HAp was reported [28].

The XRD pattern of Mg^{2+} doped HAp with PEG & CTAB are represented in Fig. 1 (b-c), respectively. The observed peaks closely resemble those of pure Mg^{2+} doped HAp, suggesting that the surfactant does not affect the crystal structure. The XRD pattern of Mg^{2+}doped HAp prepared with curcumin extract (Fig. 1(d)) also shows a similar diffraction profile observed for Mg^{2+} doped HAp without surfactant; however, the intensity gets reduced. The Debye-Scherrer equation [39] diameter measurements for pure Mg^{2+} doped HAp, Mg^{2+} doped HAp-PEG, Mg^{2+} doped HAp-CTAB and Mg^{2+} doped HAp-extract were determined to be 105 ± 6 nm, 84 ± 4 nm, 91 ± 7 nm, and 79 ± 6 nm, respectively.

Unit cell software was used to determine the lattice parameter values, which are shown in Table 1. The synthesized Mg^{2+} doped HAp's cell volume and lattice constants was found to be in good agreement with the standard data (JCPDS Card No: 09–0432) $c = 6.884$ Å, $a = 9.418$ Å, and $V = 528.80$Å^3. It is clear that the lattice properties of the Mg^{2+} doped HAp samples have good consistency with standard data and all of the parameters are in perfect agreement with the earlier reports [6,9,19,29]. Due to being sharper and more isolated from others, the diffraction peaks at (002), (211), and (300) planes were selected to calculate the crystallite size of Mg^{2+} doped HAp, as shown in Table 1. Based on the strain value, when compared to Mg^{2+}doped HAp and Mg^{2+}doped HAp-Extract nanopowder which is evident for the decrease in crystallite size [3].

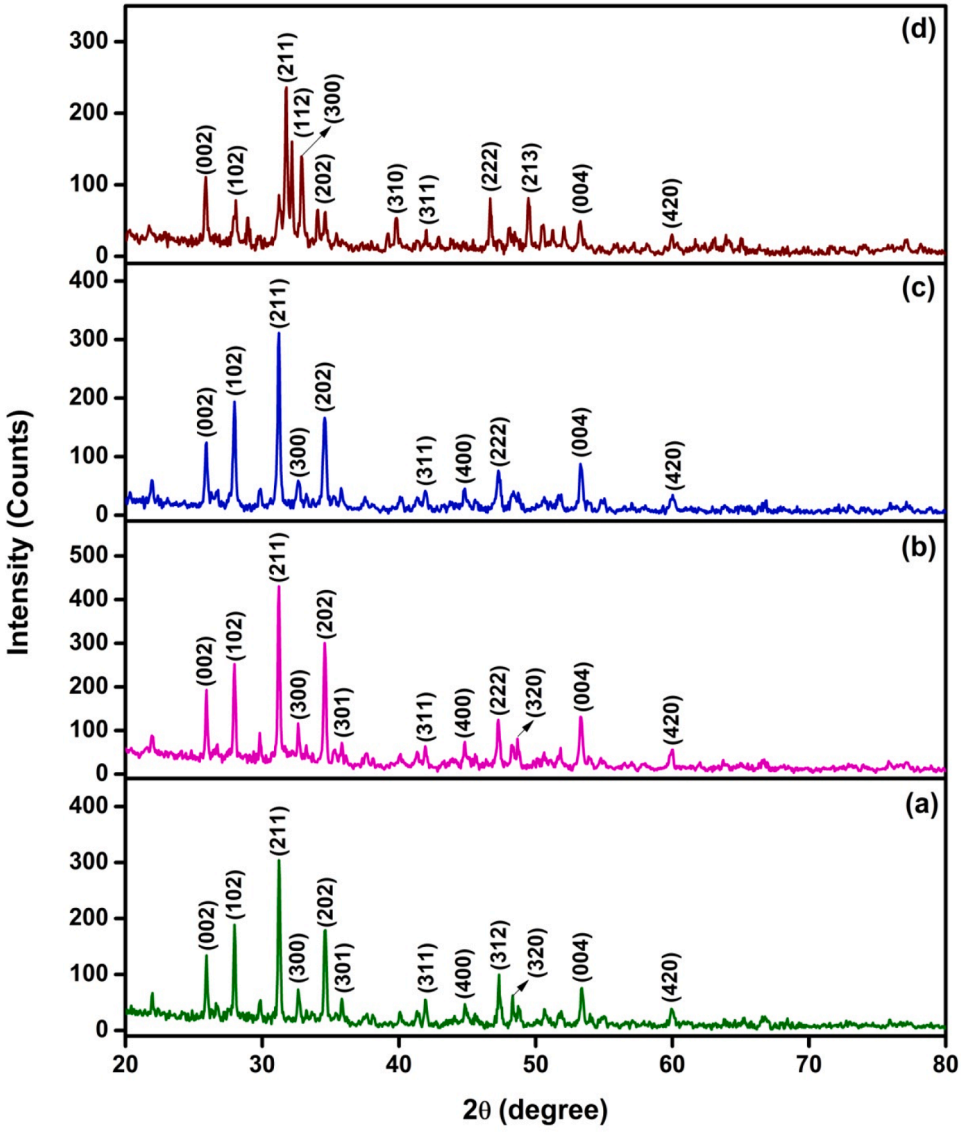

Fig. 1. XRD spectrum of Mg^{2+} doped HAp NPs calcined at 500 °C. (a) Mg^{2+} HAp, (b) Mg^{2+} HAp-PEG, (c) Mg^{2+} HAp-CTAB and (d) Mg^{2+} HAp- curcumin (JCPDS: 09–0432).

Table 1
Calculated values of Mg^{2+} doped HAp NPs calcined at 500 °C.

Samples	Crystallite Size (nm)	Dislocation density (δ) x 10^{15} (lines/m^2)	Strain (ε) x 10^{-3}	Lattice cell Parameters (Å)		Unit Cell Volume (Å)^3
				a	c	
Mg^{2+} HAp	51	0.3982	0.0394	9.3842	6.8402	521.6803
Mg^{2+} HAp-PEG	42	0.5650	0.0473	9.4379	6.8588	529.1035
Mg^{2+} HAp-CTAB	37	0.7966	0.0551	9.5037	6.8706	529.5673
Mg^{2+} HAp-curcumin extract	56	0.3163	0.0353	9.4170	6.8701	527.6231

3.2. FTIR spectroscopy

The synthesized HApNPs were subjected to FTIR analysis in order to determine their functional groups, identify any unknown species, and analyze their vibrational modes. The FTIR spectrum of HAp NPs doped with Mg^{2+} displays a range of bands that can be attributed to distinct vibrational modes (Fig. 2a-d). The spectra include samples with and without the presence of polyethylene glycol (PEG) and cetyltrimethylammonium bromide (CTAB), as well as curcumin extract. The assignments of the observed bands can be located in Table 2.

Fig 2(a) represents FTIR spectrum of pure Mg^{2+} doped HAp and the peaks at 556 cm^{-1} and 604 cm^{-1} were caused by PO_4^{3-}'s v4 bending vibrations. The peak at 924 cm^{-1} was caused by due to PO_4^{3-}'s symmetric stretching mode. Similarly, peaks at 1027 cm^{-1} and 1073 cm^{-1} were due to the asymmetric stretching mode of PO_4^{3-}. The functional group of CO_3^{2-} can be observed at 1382 cm^{-1} and may be due to contact between atmospheric carbon dioxide and the HAp precursor solution. The peaks at 3434 cm^{-1} and 1641 cm^{-1} represent the stretching mode of OH^- and bending mode of water molecules, respectively. The occurrence of both hydroxyl and phosphate vibrational modes confirmed HAp formation. The OH- bands appear even at higher temperatures because they seem to be due to the presence of water in the lattice, not the

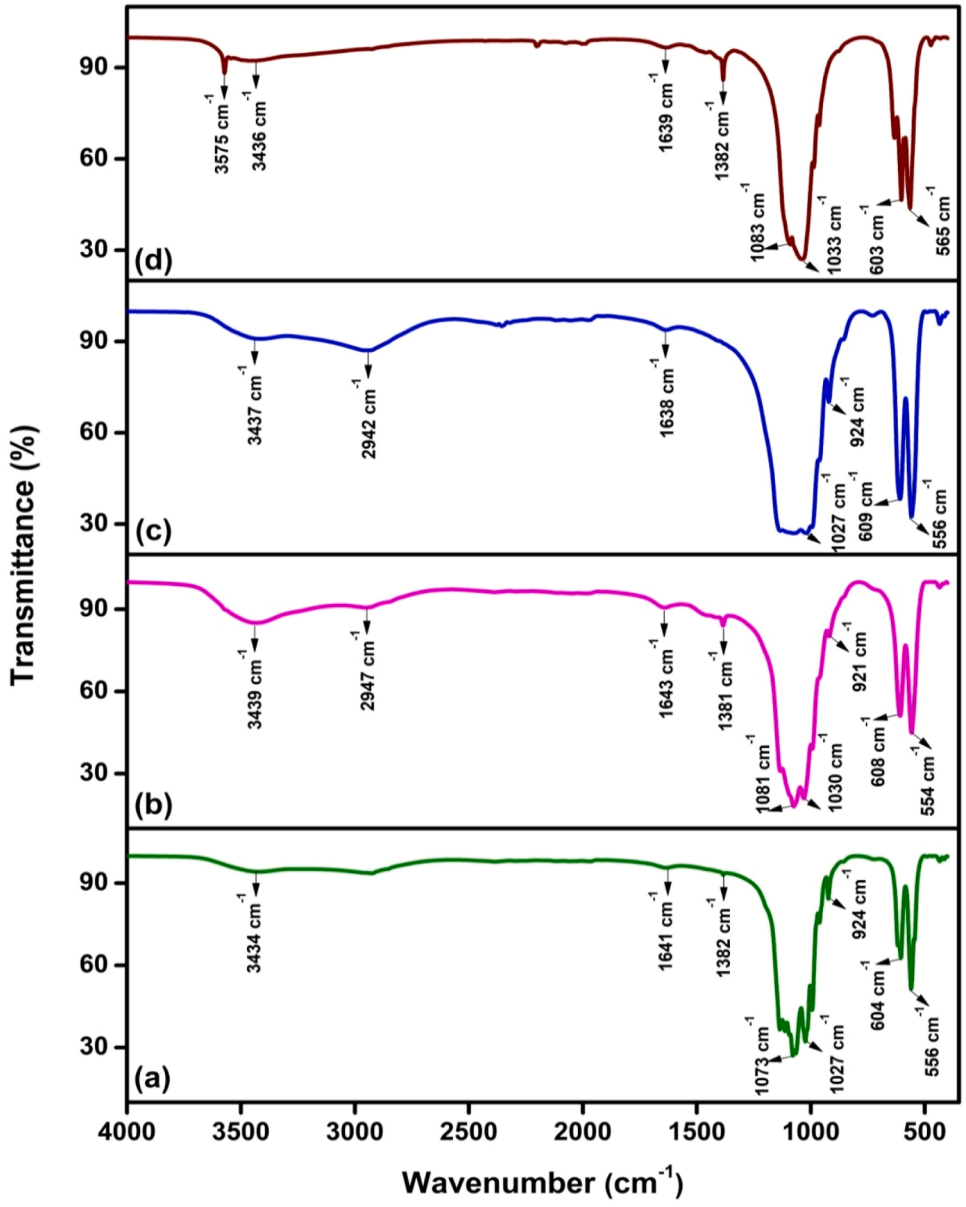

Fig. 2. FTIR band assignments of Mg^{2+} doped HAp NPs calcined at 500 °C. (a) Mg^{2+} HAp, (b) Mg^{2+} HAp-PEG, (c) Mg^{2+} HAp-CTAB and (d) Mg^{2+} HAp- curcumin.

absorbed water, because absorbed water gets removed around 100 °C.

Fig. 2 (b-c) represents the FTIR spectrum of Mg^{2+}doped HAp prepared with PEG and CTAB, respectively. When compared with pure Mg^{2+}doped HAp, preparation with PEG and CTAB exhibited similar profiles. However, few peaks are found at 2947 cm^{-1} for Mg^{2+}doped HAp-PEG and 2942 cm^{-1} for Mg^{2+}doped HAp-CTAB and these peaks are due to the presence of ν (C—H) stretching. It confirmed that the organic surfactant was not thoroughly washed from the acquired samples [32]. Similarly, Fig. 2(d) represents the FTIR spectrum of Mg^{2+} doped HAp synthesized with curcumin extract. The absorption band detected at 1382 cm^{-1} was due to the presence of ν_3 carbonate ions (CO_3^{2-}), which might be originated from the atmosphere during the preparation of samples. The absence of any alterations or emergence of additional peaks (bands) does not provide evidence of the molecular structural integrity of curcumin in the stable prepared NPs [36]. The characteristic vibration bands related to phosphate, hydroxyl, and observed water were present in the FTIR spectra of Mg^{2+}doped HAp samples. Some of the peak positions have shifted slightly compared to Mg^{2+} doped HAp, which is probably due to the interaction of surfactants PEG, CTAB, and curcumin extract. Both XRD and FTIR spectra analysis confirmed the synthesis of Mg^{2+} doped HAp.

3.3. Raman spectroscopy

In contrast to X-ray powder diffraction, Raman spectroscopy is much more sensitive to the existence of secondary phases. The synthesized Mg^{2+} doped HAp phase was analyzed by using Raman spectroscopy. At room temperature, all materials' Raman spectra originate in the 400–1500 cm-1 range. Fig. 3 (a-d) illustrates the Raman spectrum of the synthesized Mg^{2+} doped HAp NPs, both with and without surfactants. The corresponding band positions and their respective frequency assignments can be found in Table 3.

Fig. 3(a) represents the Raman spectrum of pure Mg^{2+} doped HAp NPs. The bending and stretching modes of the phosphate group were contributed from the observed vibrational bands. The asymmetric bending mode of PO_4^{3-} was detected at 574cm^{-1}. The symmetric stretching (ν_1) and bending (ν_2) modes of PO_4^{3-} were confirmed at 969 cm^{-1} and 420 cm^{-1}, respectively. The asymmetric stretching (ν_3) and

Table 2
FTIR band assignments of Mg^{2+} doped HAp NPs calcined at 500 °C.

Mg doped HAp	Mg doped HAp-PEG	Mg doped HAp-CTAB	Mg doped HAp-Extract	Band Assignment
556	554	556	565	Asymmetric bending of PO_4^{3-} (v_4)
604	608	609	603	Asymmetric bending of PO_4^{3-} (v_4)
924	921	924	–	Symmetric stretching of PO_4^{3-}(ν_1)
1027	1030	1027	1033	Asymmetric stretching of PO_4^{3-} (v_3)
1073	1081	–	1083	Asymmetric stretching of PO_4^{3-} (v_3)
1382	1381	–	1382	Carbonate ions (CO_3^{2-}) (v_3)
1641	1643	1638	1639	Symmetric bending mode of H_2O (v_2)
–	2947	2942	–	(C—H) stretching mode (ν)
3434	3439	3437	3436	O-H stretching mode
–	–	–	3575	Symmetric stretching of H_2O (v_1)

symmetric stretching (ν_1) modes of PO_4^{3-} were found at 1100 cm^{-1} and 936 cm^{-1}, respectively [12]. The Raman spectrum of Mg^{2+} doped HAp prepared with PEG/CTAB surfactant is given in Fig. 3 (b & c), which is similar to Mg^{2+} doped HAp prepared without surfactant, but the peaks are shifted towards the lower region as given in Table 3. Fig. 3(d) represents the Raman spectra of Mg^{2+} doped HAp synthesized with

Table 3
Raman band assignments of Mg^{2+} doped HAp NPs calcined at 500 °C.

Mg doped Hap	Mg doped HAp-PEG	Mg doped HAp-CTAB	Mg doped HAp-Extract	Band Assignment
420	392	394	430	Symmetric bending mode of PO_4^{3-}(ν_2)
574	559	545	590	Asymmetric bending mode of PO_4^{3-} (v_4)
640	630	613	–	Asymmetric bending mode of PO_4^{3-} (v_4)
936	921	910	–	Symmetric stretching of PO_4^{3-} (v_1)
969	961	958	961	Symmetric stretching of PO_4^{3-} (v_1)
1100	1091	1079	1075	Asymmetric stretching of PO_4^{3-} (v_3)

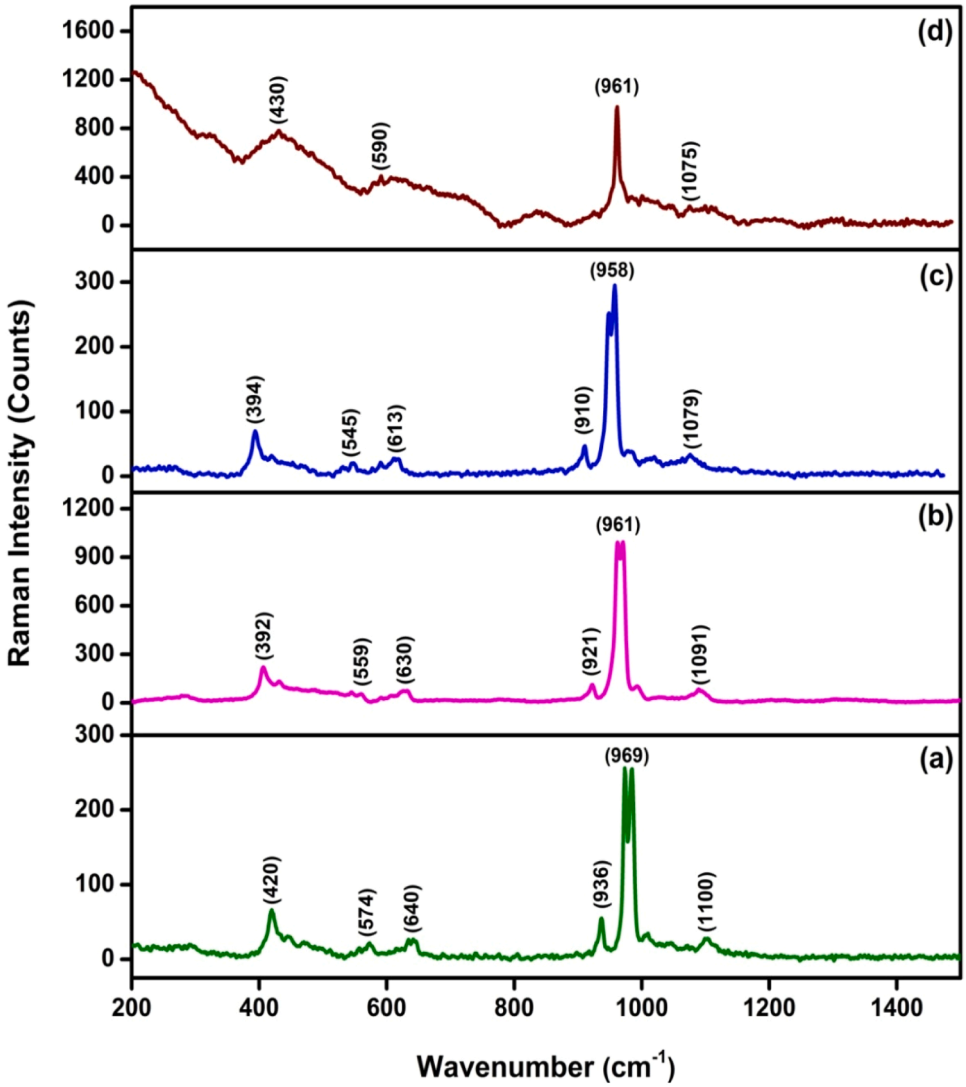

Fig. 3. Raman spectra of Mg^{2+} doped HAp NPs calcined at 500 °C. (a) pure Mg^{2+} HAp, (b) Mg^{2+} HAp-PEG, (c) Mg^{2+}HAp-CTAB and (d) Mg^{2+} HAp curcumin.

curcumin extract, and significantly, when compared with pure extract, extract preparation intensity was reduced. Therefore, the synthesis of HAp, as indicated by the XRD and FTIR methods, was validated through Raman analysis, confirming its structural characteristics.

3.4. Energy dispersive X-ray analysis

The synthesized Mg^{2+} doped HAp NPs are quantitatively analyzed for their elements using the EDAX spectra. Fig. 4 (a-d) represents the EDAX spectra of Mg^{2+} doped HAp NPs and their elemental composition are given in Table 4. The synthesis of Mg^{2+} doped HAp NPs was confirmed by the presence of P, Ca, Mg and O in the stoichiometric ratio in the EDAX spectra. No further secondary phase or impurity signal was seen in the EDAX spectra. This indicates that the processed samples are free of any contaminants. Due to equipment constraints, H could not be identified in the current study's EDAX spectra since it has an atomic number lower than five [50].

3.5. Field emission scanning electron microscopy

The FESEM images depict the NPs' shape and size distribution of the synthesized compounds. The FESEM micrograph verified the nanometric size of the particles. Fig. 5 (a-d) represents the FESEM micrographs of prepared Mg^{2+} doped HAp with or without surfactant. Fig. 5 (a) showed the images of pure Mg^{2+} doped HAp as cube-shaped particles with 105 ± 8 nm of mean diameter. The obtained nanocubes were slightly agglomerated and the distribution was not uniform. The FESEM images of Mg^{2+} doped HAp-PEG are represented in Fig. 5(b). The findings indicated that nanocubes exhibited a high level of density and a uniform arrangement. The Mg^{2+} doped HAp-PEG showed excellent dispersibility and uniformity in terms of size, with a mean diameter of approximately 85 ± 4 nm. This observation indicated that the addition of PEG resulted in a reduction in the size of the nanocubes obtained.

Table 4
Elemental compositions of Mg^{2+} doped HAp NPs calcined at 500 °C.

Samples	Calcium (Atomic%)	Oxygen (Atomic%)	Phosphate (Atomic%)	Magnesium (Atomic%)
Mg HAp	9.94	79.32	9.49	1.24
Mg HAp-PEG	164	73.63	9.86	0.87
Mg HAp-CTAB	22.82	61.52	14.43	1.24
Mg HAp-Extract	28.59	59.08	10.35	1.98

Fig. 5 (c-d) shows slightly agglomerated and highly agglomerated spheres of Mg^{2+} doped HAp prepared with CTAB as surfactant and curcumin extract assisted, respectively. When CTAB is used as a surfactant, the obtained spheres are evenly distributed and uniform in size. The mean diameter of Mg^{2+} doped HAp-CTAB were approximately 95 ± 4 nm. But, the curcumin-assisted Mg^{2+} doped HAp shows highly agglomerated and disoriented spheres with a mean diameter of 78 ± 5 nm.

Approximately 100 particles from each of the four FESEM images were randomly chosen for statistical analysis based on their significance level. The three population means of distinct pure Mg^{2+} doped HAp, Mg^{2+} doped HAp-PEG, Mg^{2+} doped HAp-CTAB and Mg^{2+} doped HAp-extract were constructed with a 95 % confidence level, and they were primarily within the range of (− 2.277, 2.227), (−0.889, 0.889) and (−0.558, 0.558), respectively. According to the statistical analysis, there was no significant difference in the size of Mg^{2+} doped HAp caused by the alteration procedure. Importantly, values obtained from XRD image analysis were in agreement with the distribution of size analysis from FESEM image measurements of the particles overall mean diameter.

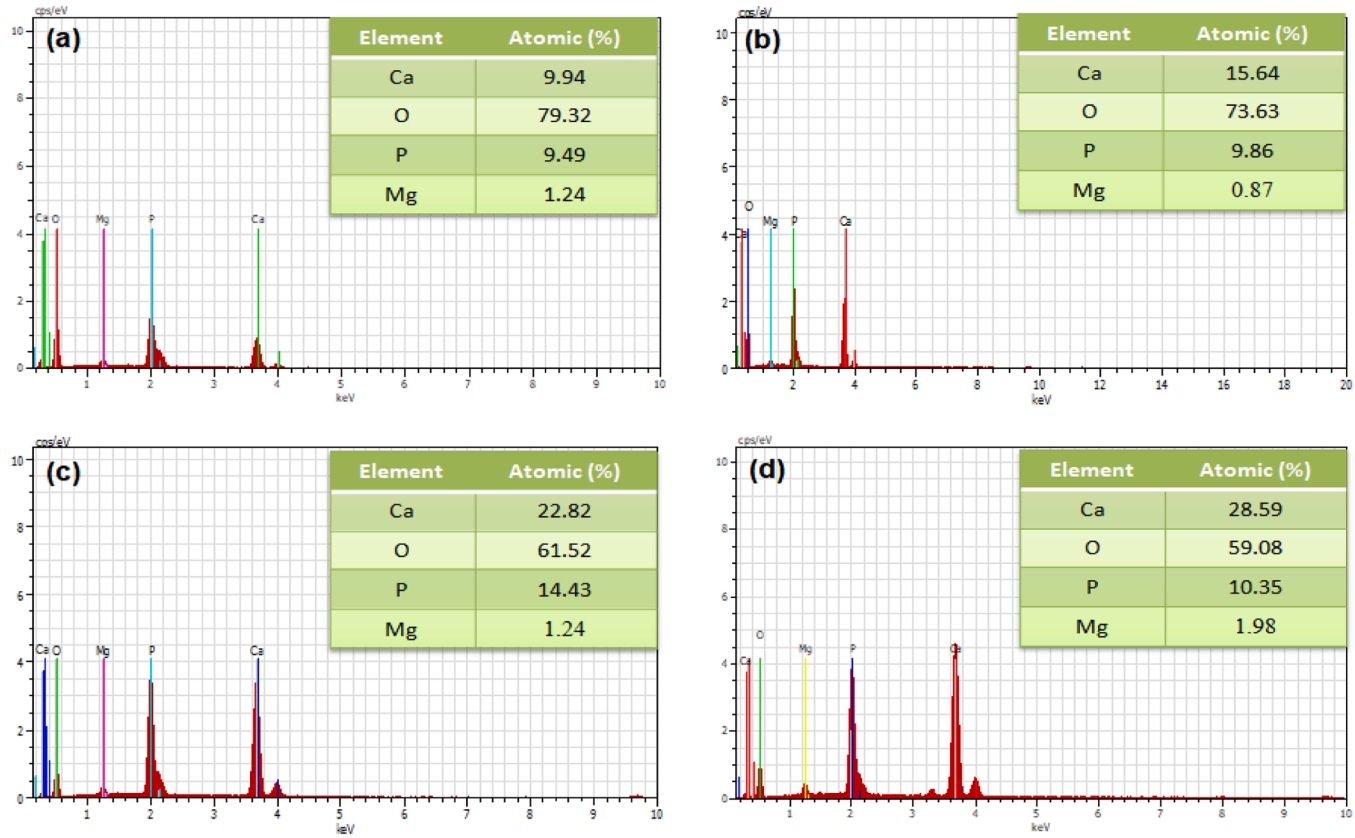

Fig. 4. EDAX spectra of Mg^{2+} doped HAp NPs calcined at 500 °C. (a) pure Mg^{2+} HAp, (b) Mg^{2+} HAp-PEG, (c) Mg^{2+}HAp-CTAB and (d) Mg^{2+} HAp curcumin.

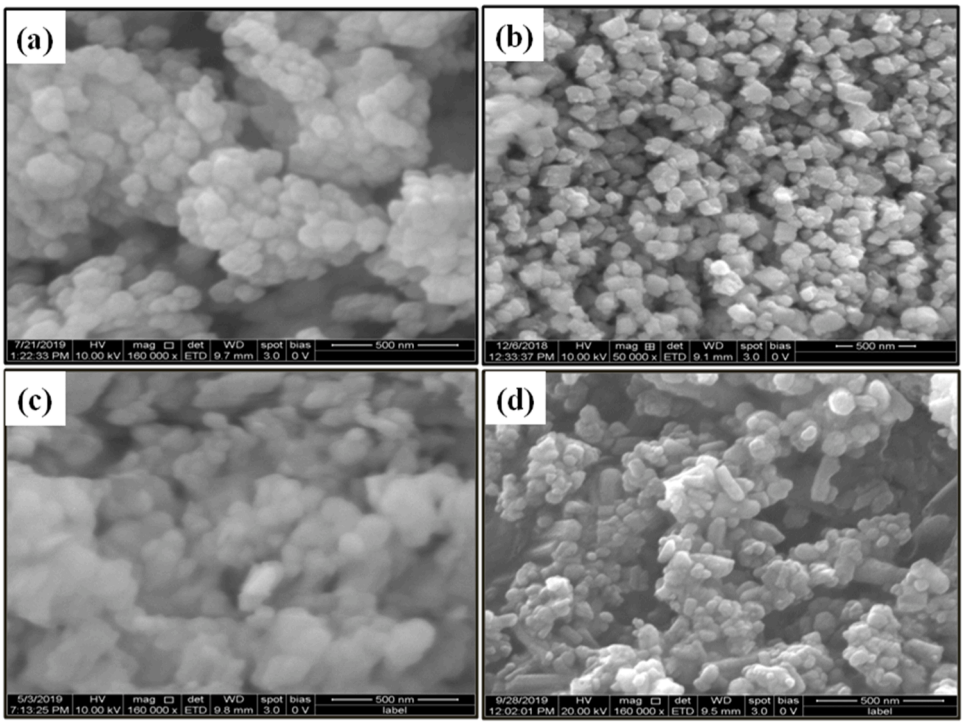

Fig. 5. FE-SEM images of Mg^{2+} doped HAp NPs with a magnification at 500 nm. (a) pure Mg^{2+} doped HAp, (b) Mg^{2+} doped HAp-PEG, (c) Mg^{2+} doped HAp-CTAB and (d) Mg^{2+} doped HAp-curcumin.

3.6. Transmission electron microscope

TEM pictures were captured for a more thorough structural investigation of Mg^{2+} doped HAp. Fig. 6 (a-f) shows a schematic representation of pure Mg^{2+} doped HAp NPs at various magnifications. About 116 nm of diameter cubic-shaped NPs with a uniform microstructure was observed. The hexagonal phase of Mg^{2+} doped HAp was detected together with the well-defined and clear diffraction rings. According to the strength of the diffraction rings, the particles were well-crystalline and had a restricted size range. The presence of an SAED pattern exhibiting distinct circular rings that correspond to the observed diffraction peaks of hexagonal HAp provides evidence for the crystalline nature of magnesium-doped HAp.

3.7. UV-DRS analysis

UV-DRS spectroscopy examined the optical characteristics of Mg2+ doped HAp NPs. The absorbance and reflectance spectra are presented in

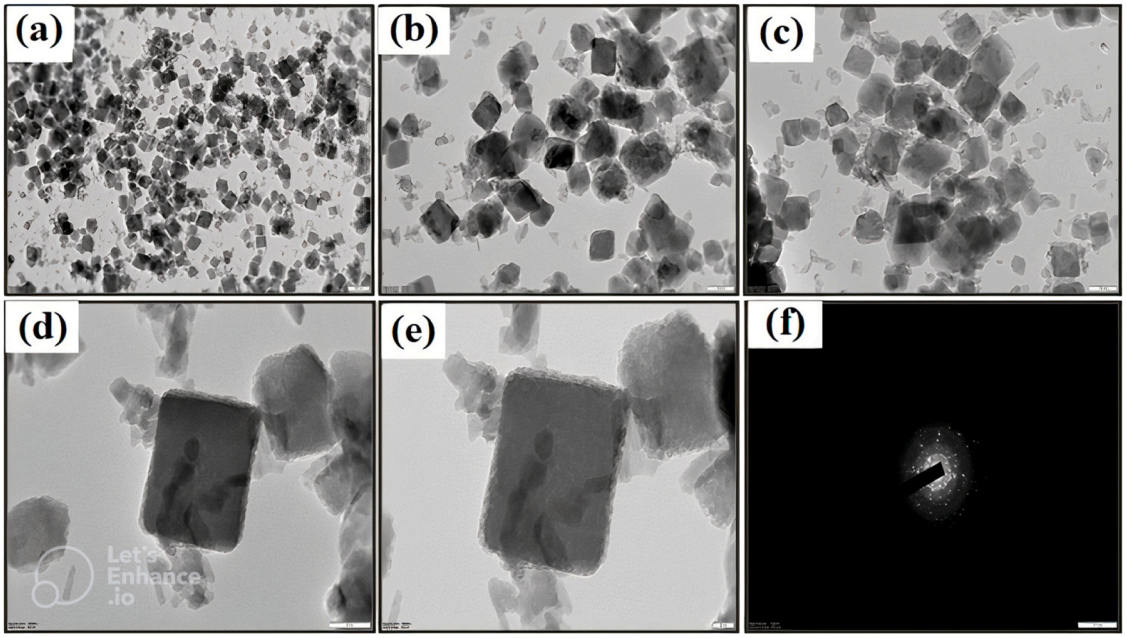

Fig. 6. TEM images for Mg^{2+} doped HAp NPs calcined at 500 °C with a magnification at (a) 200 nm, (b) 100 nm, (c) 100 nm, (d) 50 nm, (d) 20 nm and (f) SAED pattern.

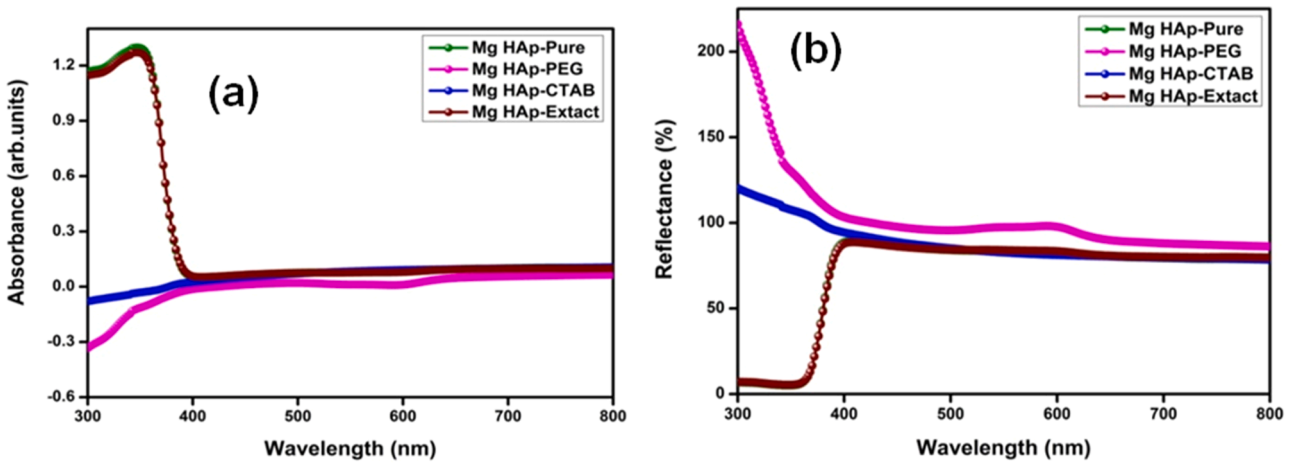

Fig. 7. (a) Absorption spectra (b) Reflectance spectra of Mg^{2+} doped HAp.

Fig. 7 (a-b). The UV-DRS spectra for Mg^{2+} doped HAp NPs are shown in Fig. 10(a), and they exhibit bandgap-related absorption in the low wavelength (UV) region between 350 and 400 nm. Due to larger crystallite size, pure Mg^{2+} doped HAp and curcumin extract exhibited optical absorption peaks in the 300–400 nm range compared to other samples.

According to the KM plot and shown in Fig. 8 (a-d), the optical band gap (Eg) of the Mg^{2+} doped HAp NPs was estimated. The modified Kubelka-Munk function [F(R) hv]2 vs photon energy (hv) graph's linear section is extrapolated to get the bandgap energy of the samples. The band values of Mg^{2+} doped HAp, Mg^{2+} doped HAp-CTAB, Mg^{2+} doped HAp-PEG, and Mg^{2+} doped HAp-Extract were found to be 3.4 eV, 3.18 eV, 4.07 eV, and 3.39 eV respectively. These samples have an estimated bandgap that is somewhat less (5 eV) than the bulk HAp sample. Due to the smaller crystallite size, it was observed that Mg^{2+} doped HAp-CTAB and Mg^{2+} doped HAp-Extract have lower bandgap values than Mg^{2+} doped HAp-PEG and pure Mg^{2+} doped HAp.

Due to the surfactants' ability to cause the development of intermediate surface defect states in the bandgap area, the optical band gap increased in HAp-PEG with Mg^{2+} doped [18]. Compared to pure HAp, lower band gap values were reported in the Mg^{2+} doped HAp-CTAB sample. According to density functional theory, the band gap value of HAp has been calculated to be between 23 and 40 eV, while actual band gap values have been reported to vary between 3.45 and 5.78 eV [26].

3.8. Photoluminescence analysis

The photoluminescence spectra of Mg^{2+} doped HAp NPs that were prepared were recorded in Fig. 9 (a-d) at ambient temperature. The same excitation wavelength of 320 nm was utilized for all the samples.

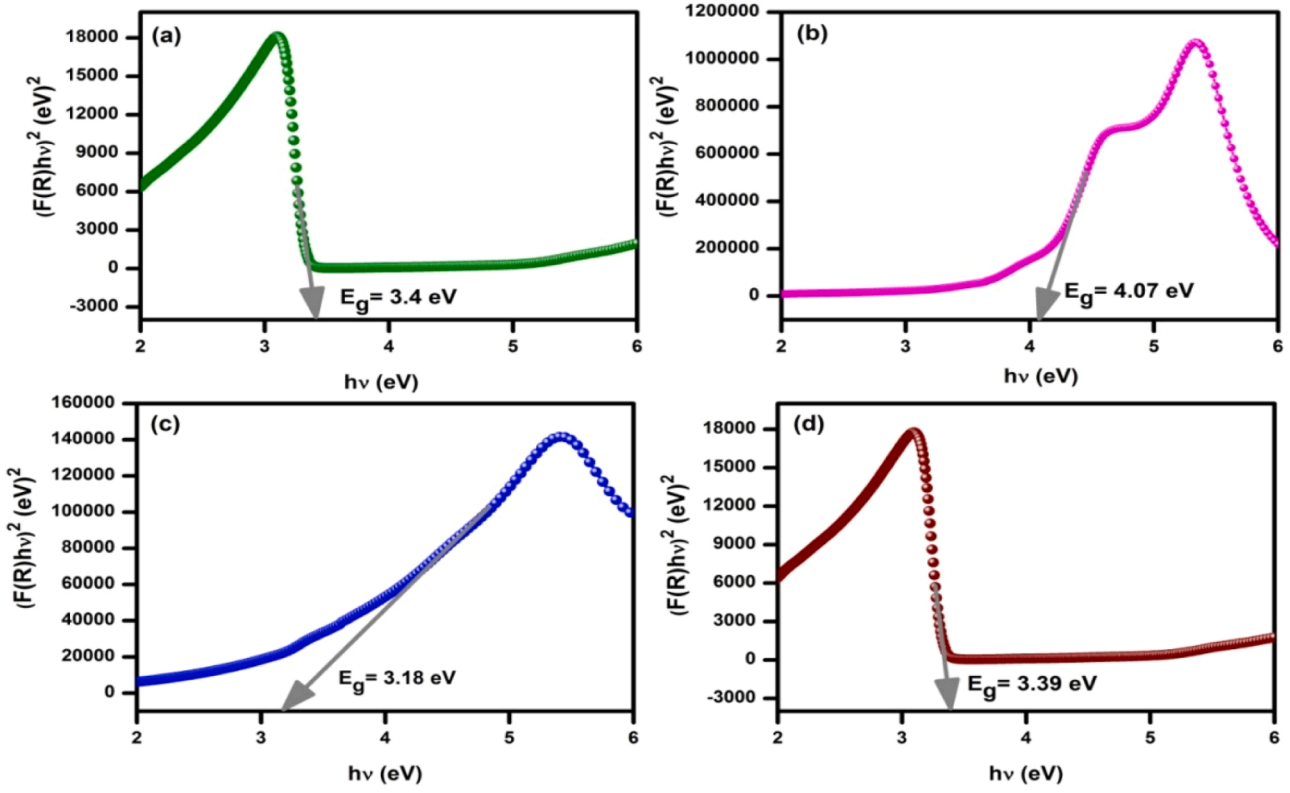

Fig. 8. KM plot for Mg^{2+} doped HAp NPs calcined at 500 °C. (a) Mg^{2+} HAp, (b) Mg^{2+} HAp-PEG, (c) Mg^{2+}HAp-CTAB and (d) Mg^{2+} HAp curcumin.

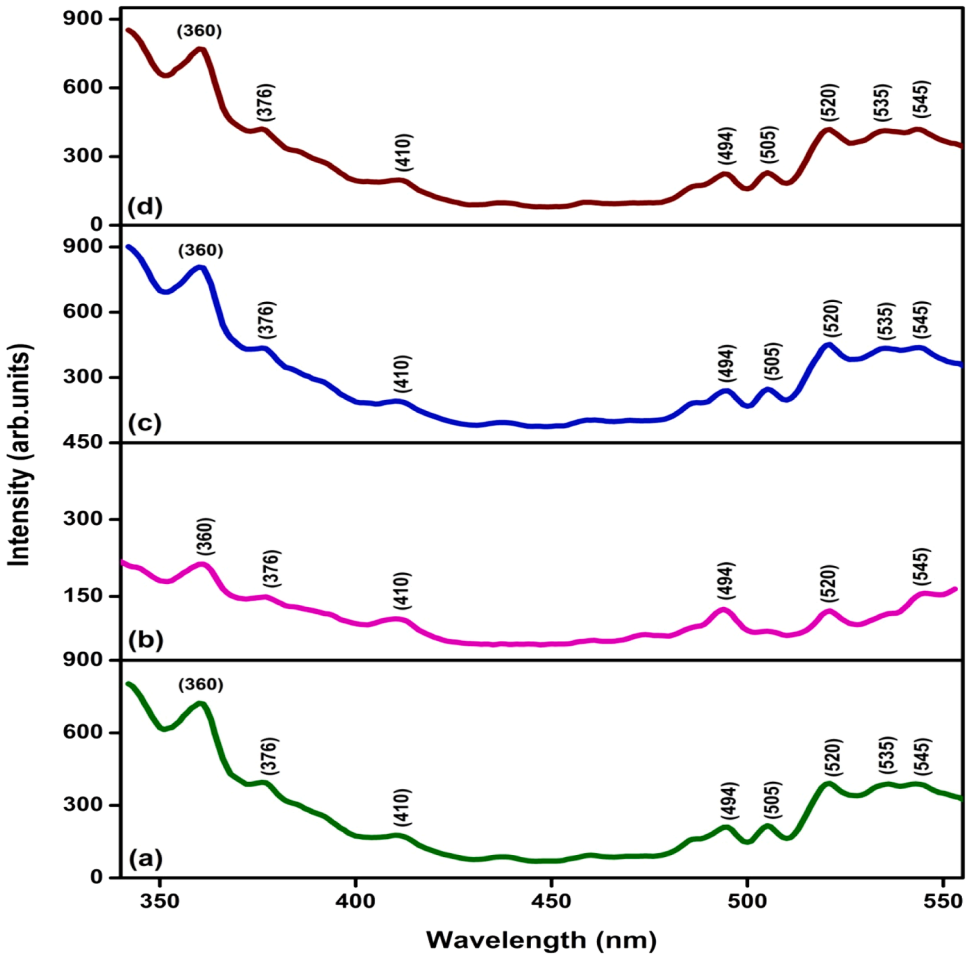

Fig. 9. Photoluminescence spectra for Mg^{2+} doped HAp NPs with an excitation wavelength of 320 nm (a) Mg^{2+} HAp, (b) Mg^{2+} HAp-PEG, (c) Mg^{2+}HAp-CTAB and (d) Mg^{2+} HAp curcumin.

The emission peaks of Mg^{2+} doped HAp NPs range from a minimum wavelength of 350 nm to a maximum wavelength of 550 nm. The samples Mg^{2+} doped HAp, Mg^{2+} doped HAp-CTAB, and Mg^{2+} doped HAp-Extract exhibit emission peaks at wavelengths of 360 nm, 376 nm, 410 nm, 494 nm, 505 nm, 520 nm, and 545 nm. For Mg^{2+} doped HAp-PEG, identical emission peaks were observed; however, a peak at 505 nm was disappearing. Four distinct and powerful emission bands comprised the PL emission. Blue emission at around 410 nm and UV radiation at about 360 nm were recorded. Surface defects cause the high blue emission peaks in the visible spectrum that occur at approximately 494 nm and 520 nm. The bandgap fluctuation recorded in UV-DRS showed that the Mg^{2+} doped HAp considerably increases the intensity of the emission peak [35].

3.9. Toxicity assay of Mg^{2+}doped HAp NPs

A toxicity assay was carried out for the synthesized Mg^{2+} doped HAp NPs prepared with or without surfactant for various concentrations such as 50 μl (c1), 75 μl (c2), and 100 μl (c3) are given in Fig. 10. It is observed from the Fig. 10, no zone of inhibition was recorded for all the prepared samples, revealing the non-toxic nature of Mg^{2+} doped HAp. Due to its non-toxic and eco-friendly nature, it can be used as biomaterials for the remediation of human pathogens and cancer cells.

3.10. Antibacterial activity of Mg^{2+}doped HAp NPs

Mg^{2+} doped HAp NPs have unique characteristics that prompted the investigation of their biological functions. The well diffusion assay

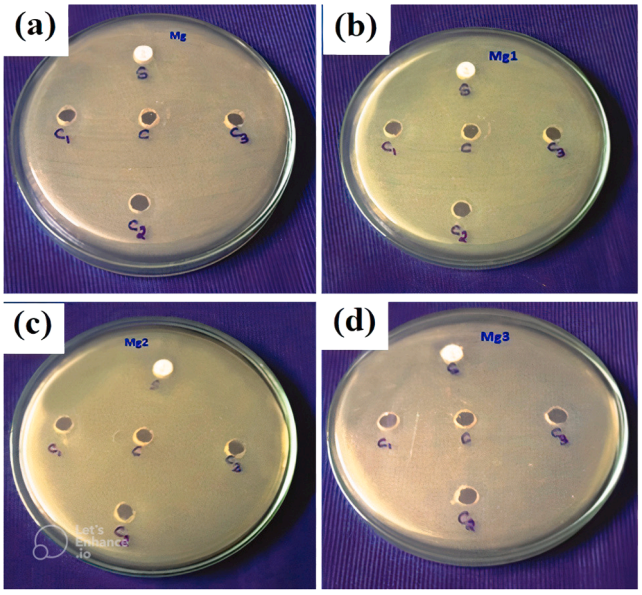

Fig. 10. Toxicity assay of Mg^{2+} doped HAp NPs calcined at 500 °C. (a) Mg^{2+} doped HAp, (b) Mg^{2+} doped HAp-PEG, (c) Mg^{2+} doped HAp-CTAB and (d) Mg^{2+} doped HAp- curcumin.

technique was used to test in-vitro the antibacterial activity of all synthesized particles. All Mg^{2+} doped HAp NPs were tested for their ability to inhibit the growth of human pathogens. Microorganisms such as *E. coli* (MTCC-4213), *Shigella flexneri* (MTCC-2197), *Pseudomonas aeruginosa* (MTCC-3131), *Klebseilla pneumoniae* (MTCC-1214) and *Staphylococcus aureus* (MTCC-3123) were used in this study. The measurement of the sample's ability to inhibit a specific microorganism is determined by its zone of inhibition. This refers to the area where bacterial growth is prevented due to the sample's bacteriostatic properties.

Five different bacterial strains' zones of inhibition were measured, and the results are shown in Fig. 11. Inhibition zone sizes are shown in Fig. 12. At a concentration of 50 μg, all the samples were at their most effective. Inhibition zones were largest against *Shigella flexneri* when using Mg^{2+} doped HAp with PEG surfactant (Mg1) was used. CTAB-assisted Mg^{2+} doped HAp (Mg2) NPs showed a minimal zone of inhibition about 15 mm against *Shigella flexneri*, whereas pure Mg^{2+} doped

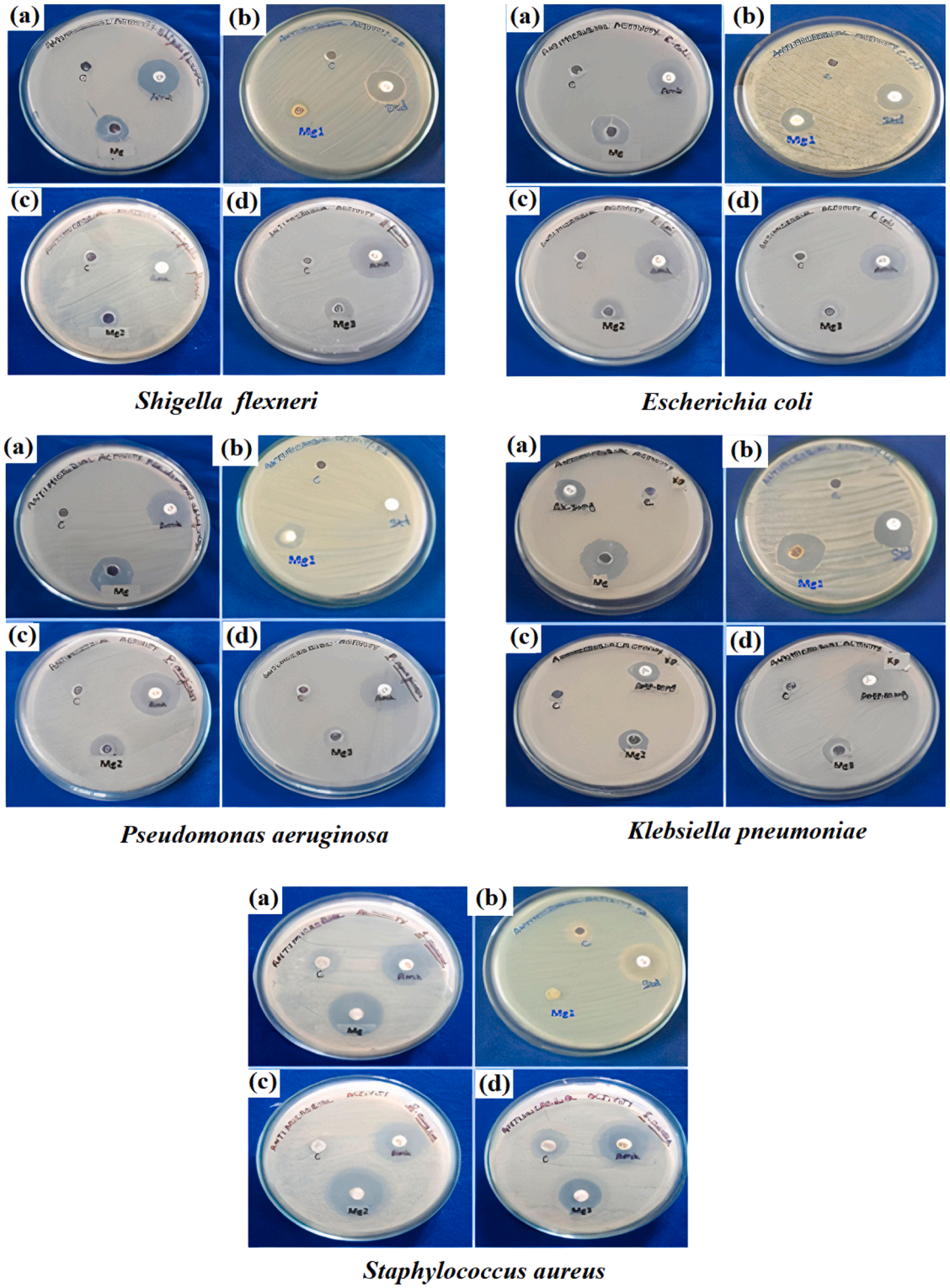

Fig. 11. Mg^{2+}-doped HAp NPs' antibacterial activity against selective microorganism (a) Mg HAp, (b) Mg HAp-PEG, (c) Mg HAp-CTAB and (d) Mg HAp- curcumin.

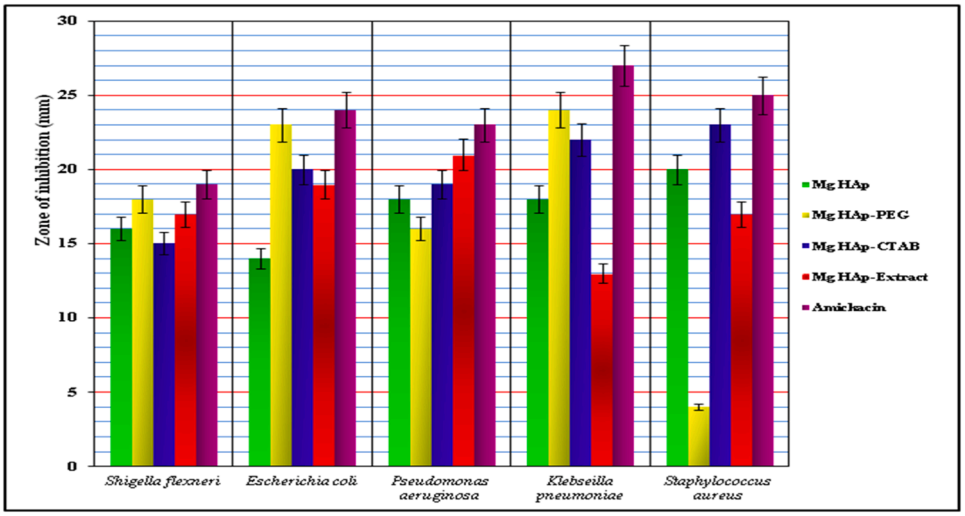

Fig. 12. Antibacterial activity of Mg^{2+} doped HAp NPs treated against bacterial pathogens.

HAp NPs (Mg2) and with curcumin extract (Mg, Mg3) showed a considerable growth-inhibitory impact.

The measured zone of inhibition for *E. coli* is 14, 23, 20, and 19 mm, while for *Klebsiella pneumoniae* it is 18, 24, 22, and 13 mm for the Mg, Mg1, Mg2, and Mg3 samples, respectively. The utilization of Mg^{2+} doped HAp-PEG (referred to as Mg1) has demonstrated a significant inhibitory effect on bacterial growth, particularly for bacterial pathogens such as *E. coli* and *K. pneumoniae*.

The antibacterial activity of Mg^{2+} doped HAp against *Pseudomonas aeruginosa* is 18, 16, 19, 21 mm for Mg, Mg1, Mg2, and Mg3 samples, respectively. However, Mg^{2+} doped HAp with curcumin assisted (Mg3) demonstrated a maximal zone of inhibition close to the standard Amikacin, at around 21 mm. This finding further proves that Mg^{2+} doped HAp (curcumin) synthesized in the green has potent antibacterial action against *Pseudomonas aeruginosa*.

The strain of *Staphylococcus aureus* showed a zone of inhibition of 23, 3, 20, 23 mm for Mg, Mg1, Mg2, and Mg3 samples, respectively. Similarly, pure Mg^{2+} doped HAp (Mg) and Mg^{2+} doped HAp with curcumin extract (Mg3) showed identical and extreme zone of inhibition around 23 mm. An inhibition zone of about 20 mm was recorded with Mg^{2+}-doped HAp with CTAB (Mg2), whereas Mg^{2+}-doped HAp with PEG (Mg1) exhibited very little inhibitory potential. CTAB is a promising antimicrobial agent often used for disinfection and sanitation purposes. This chemical is deemed to be reasonably safe and is cost-effective for the purpose of sterilizing rooms. The ongoing epidemic has created a pressing need and high demand for medicines targeting novel and/or overlooked disease-causing chemicals. CTAB is a prominent chemical used for extracting nucleic acid from bacteria, fungi, plants, viruses, and pneumonia-causing pathogens. It has antiviral characteristics in this context. This chemical has also been discovered to enhance cell lysis by damaging the membrane of the viral particle [34]. These properties of CTAB have inspired to develop Mg^{2+} doped HAp incorporated with CTAB. Therefore, the prospective applications of Mg^{2+} doped HAp NPs in the biomedical sector are expanded due to their high antibacterial activity. Additionally, the beneficial effect of PEG in increasing its antibacterial activity is due to the adverse influence of PEG on the fabric surface, which disrupts the equilibrium of the cell membrane in bacteria. This disruption results in a combination of hydrophobic and hydrophilic properties, ultimately leading to the drying out of the microbes [20].

Bacterial species are often anticipated to have localized interactions with nanoscale particles of Mg^{2+} doped HAp and are capable of strongly adhering to the extensive surface of the coatings. This close contact might enhance the antibacterial effect of synthesized Mg^{2+} doped HAp NPs [41]. Recently, zinc and gallium-doped HAPs NPs exhibited anti bacterial activity against *Staphylococcus aureus* and *E. coli* [47]. The bactericidal activity can potentially be considerably influenced by the concentration of nanopowders, in addition to ion doping and bacteria strains. Hence, further research is required to study the interaction of various concentrations of synthesized Mg^{2+} doped HAp NPs.

3.11. *Antifungal activity of Mg^{2+}doped HAp NPs*

Fig. 13 represents the results of antifungal activity analysis of Mg2+ doped HAp NPs against the pathogenic fungi *Aspergillus niger, Odium caricae* and *Aspergillus flavus*. Fig. 14 both shows the measurement of the zone of inhibition. The acquired antifungal activity was compared with the standard antibiotic of Clotrimazole. It was found that samples of (Mg, Mg1, Mg2, and Mg3) exhibited moderate and least activity at the concentration of 20, 30, and 40 µg. However, the concentration at 50 µg showed the highest antifungal activity.

The zone of inhibition of 26, 21, 21, and 22 mm against *Odium caricae* demonstrated the antifungal activity of Mg, Mg1, Mg2, and Mg3 samples. The pure Mg^{2+} doped HAp (Mg) had the greatest antifungal efficacy of the four samples; however, Mg^{2+} doped HAp with curcumin extract (Mg3) showed a modest zone of inhibition. An equal and minimal zone of inhibition was found for Mg1 and Mg2 samples with 21 mm of zone of inhibition.

For *A. niger*, the zone of inhibition for the Mg, Mg1, Mg2, and Mg3 samples were 24, 19, 26, and 23 mm, respectively. Mg^{2+}doped HAp NPs synthesized with CTAB surfactant (Mg2) showed a significant inhibitory effect. The maximum antifungal activity against *A.niger* was recorded for Mg^{2+} doped HAp with CTAB and compared to the common antibiotic clotrimazole, which is an exciting outcome from the current investigation.

The maximum zone of inhibition for Mg^{2+} doped HAp without surfactant (Mg) was about 24 mm and similarly, Mg^{2+} doped HAp with extract (Mg3) showed a moderate value with 23 mm zone of inhibition. Conversely, the Mg1 sample exhibited less activity with a 19 mm zone of inhibition.

For the Mg, Mg1, Mg2, and Mg3 samples, the zones of inhibition against *A. flavus* were determined to be 23, 9, 20, and 19 mm, respectively. Interestingly, samples of Mg and Mg2 exhibited around 23 mm and 20 mm zone of inhibition against *A. flavus*. Samples of Mg3 and Mg1 exhibited about 19 mm and 9 mm zone of inhibition. Thus, Mg and Mg2 exhibited the maximum antifungal activity and have stronger antifungal activities.

The antifungal activity of synthesized Mg^{2+} doped HAp NPs might be due the interaction with the fungal cell membrane. This interaction

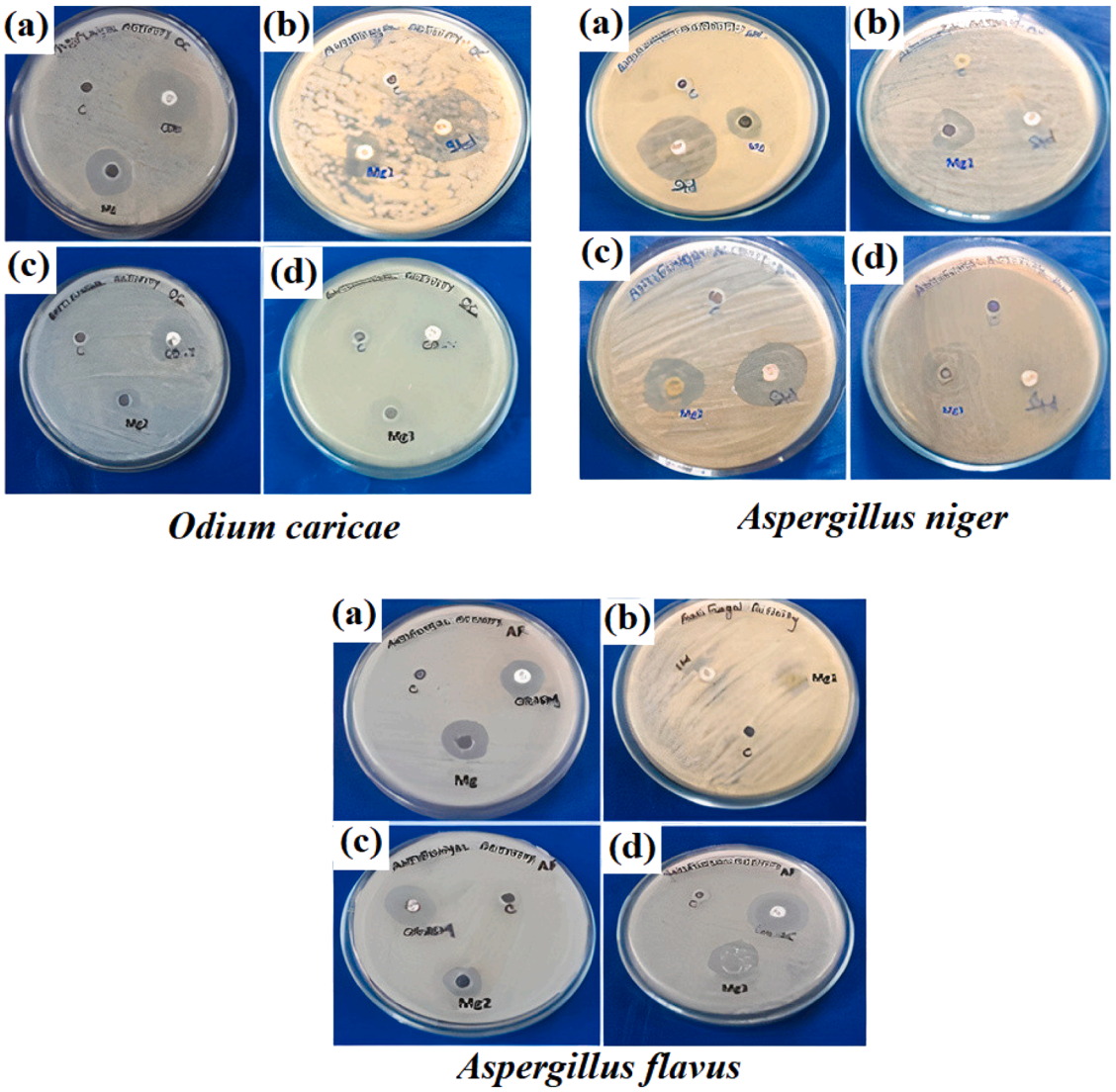

Fig. 13. Antifungal activity of Mg^{2+}doped HAp NPs treated against selected fungi (a) Mg^{2+} HAp, (b) Mg^{2+} HAp-PEG, (c) Mg^{2+} HAp-CTAB and (d) Mg^{2+} HAp-curcumin. (a) Mg HAp, (b) Mg HAp-PEG, (c) Mg HAp-CTAB and (d) Mg HAp-Extract.

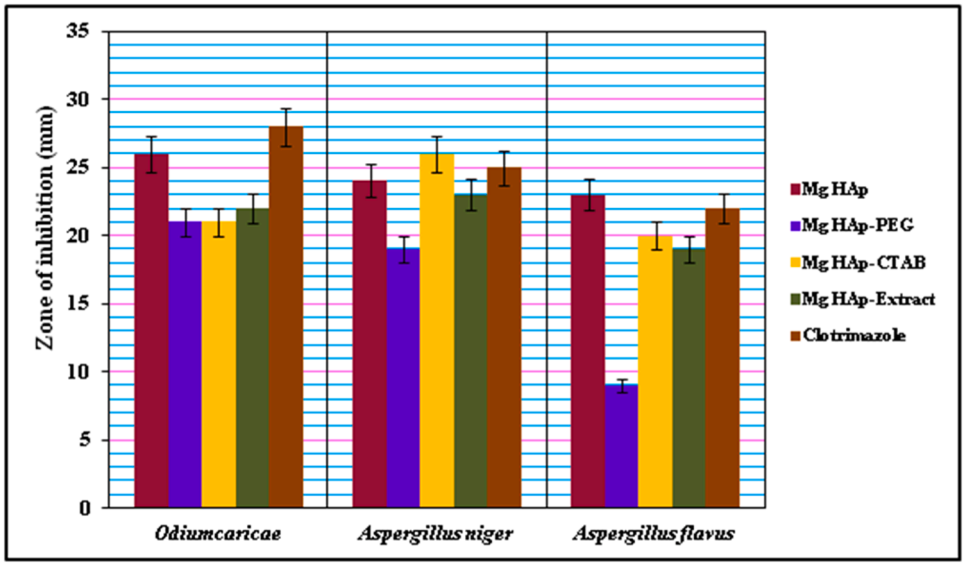

Fig. 14. Antifungal activity of Mg^{2+}doped HAp NPs treated against fungal pathogens.

results in structural damage to the membrane and ultimately leads to the death of the cell [21]. Recently, cerium-doped hydroxyapatite exhibited antifungal activity against *Candida albicans* [21]. Similarly, Europium-doped hydroxyapatite showed antifungal activity against *Candida albicans* [10]. Consequently, the findings indicated that the creation of innovative Mg^{2+} doped HAp NPs has the potential to produce very effective antifungal agents.

3.12. Antioxidant activity of synthesized Mg^{2+} doped HAp NPs

The DPPH analysis revealed that Mg^{2+} doped HAp nanoparticles had increased free radical scavenging activity. The concentrations were varied from 100 to 400 μg/mL. The graph in Fig. 15 shows that the samples' free radical scavenging effectiveness improves as their concentration increases. Notably, curcumin extract of Mg^{2+} doped HAp in all doses demonstrated the best scavenging efficiency, whereas conventional Rutin only displayed 60 % scavenging activity at all tested concentrations (100–400 μg/mL). Thus, it can be predicted that Mg^{2+} doped HAp nanoparticles containing curcumin extract have strong antioxidant activity, which may defend the human body from dangerous illnesses.

3.13. Cytotoxic activity of synthesized Mg^{2+} doped HAp NPs

Using the MTT assay, the cytotoxic impact of Mg^{2+} doped HAp was assessed on the grown HeLa cell line, and the anticancer pictures are shown in Fig. 16. It was also tested with or without surfactants as well as with curcumin extract assisted Mg^{2+} doped HAp. The concentrations of Mg^{2+} doped HAp nanoparticles, which are shown in Fig. 17, affected the viability of the cells. All Mg^{2+} doped HAp samples exhibited high cytotoxicity against the selected cell lines. The size of the nanoparticles and the kind of cell determine whether Mg^{2+} doped HAp nanoparticles are cytotoxic. For the higher concentration of 100 μg/mL of HAp without surfactant, the cell viability was reported to be 18.82 %, but for Mg^{2+} doped HAp at 50 μg/mL, 25 μg/mL, 12.5 μg/mL, and 6.25 μg/mL, it was 41.17 %, 63.52 %, 82.35 %, and 91.76 %, respectively. The synthesized Mg^{2+} doped HAp nanoparticles had to be present in at least 100 μg/mL concentrations to kill 30 % of the cells. Hydroxyapatite has been used for hip, bone, and dental replacements. HAp has several exceptional characteristics, such as increased osteoconductivity and osteoinduction upon implantation in the human body [52]. The synthesized Mg^{2+} doped HAp exhibited cytotoxic activity, possibly attributed to its capacity to induce apoptosis in HeLa cells. This apoptotic effect seems to be influenced by the concentration of Mg^{2+} doped HAp [52]. Subsequently, the composite of Mg^{2+} doped HAp nanoparticles can serve as a viable material for targeted therapy of tumor cells.

Mg^{2+} doped HAp with surfactant PEG has shown the cell viability as 31.18 %, 50.53 %, 74.19 %, 82.79 % and 94.62 %, respectively, for the concentrations 100 μg/mL, 50 μg/mL, 25 μg/mL, 12.5 μg/mL and 6.25 μg/mL. When used against HeLa cell lines, Mg^{2+} doped HAp with CTAB and curcumin extract aided Mg^{2+} doped HAp showing a comparable impact on cell survival. The dose required to reduce the development of tumour cells in culture by 50 % from that of untreated cells is known as the half-maximal inhibitory concentration (IC_{50}) [16]. With IC_{50} values of 44.309 μg/mL, 58.326 μg/mL, 63.788 μg/mL, and 74.895 μg/mL, respectively, against HeLa cell lines, all the synthesized Mg^{2+} doped HAp samples (Mg, Mg1, Mg2, Mg3) exhibited cytotoxic activity.

4. Conclusion

The Mg^{2+} doped HAp, Mg^{2+} doped HAp-PEG, Mg^{2+} doped HAp-CTAB, and Mg^{2+} doped HAp curcumin were all prepared using the sol-gel method. Subsequent characterization of the synthesized nanoparticles was conducted. The transmission electron microscopy images provided evidence of the presence of cubic-shaped particles in the magnesium-doped hydroxyapatite nanoparticles. The EDAX spectrum exhibited a stoichiometric nature for all samples, with no additional indications of impurities detected. Curcumin was successfully incorporated with prepared Mg^{2+} doped HAp and showed highly agglomerated and disoriented spheres with a 75–80 nm diameter. Further, among the NPs, Mg^{2+} doped HAp curcumin had improved antibacterial and antioxidant activity, which ensures significant potential for utilization in the biomedical domain. The HAp samples doped with Mg^{2+} exhibited notable cytotoxicity against HeLa cell lines. Additional in vivo experiments will be conducted using a suitable animal model. The results of this work suggest that using various surfactants in the production of Mg^{2+} doped HAp nanoparticles renders these particles appropriate for biomedical applications.

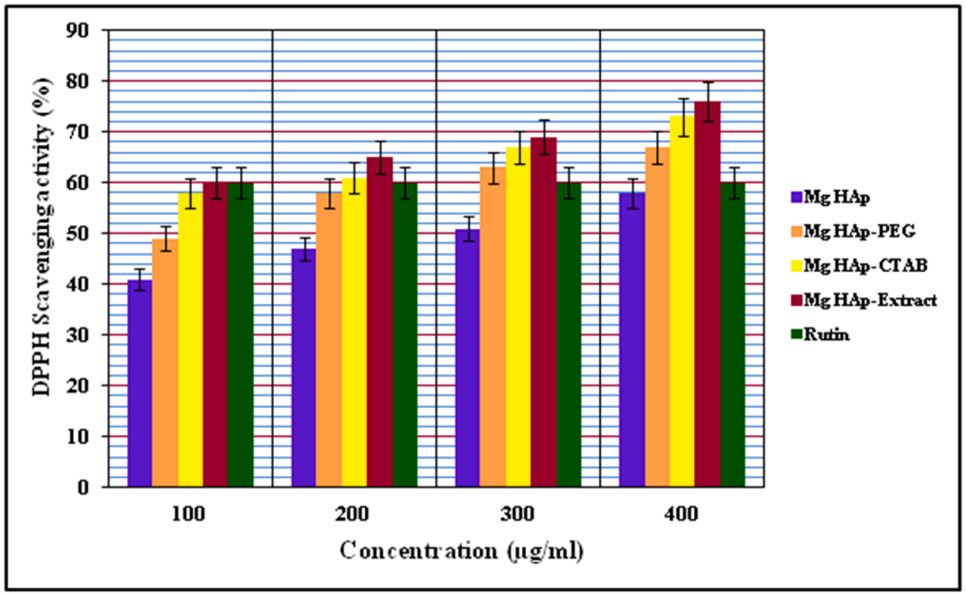

Fig. 15. Antioxidant Activity of Mg^{2+} doped HAp NPs calcined at 500 °C. (a) Mg^{2+} HAp, (b) Mg^{2+} HAp-PEG, (c) Mg^{2+} HAp-CTAB and (d) Mg^{2+} HAp- curcumin.

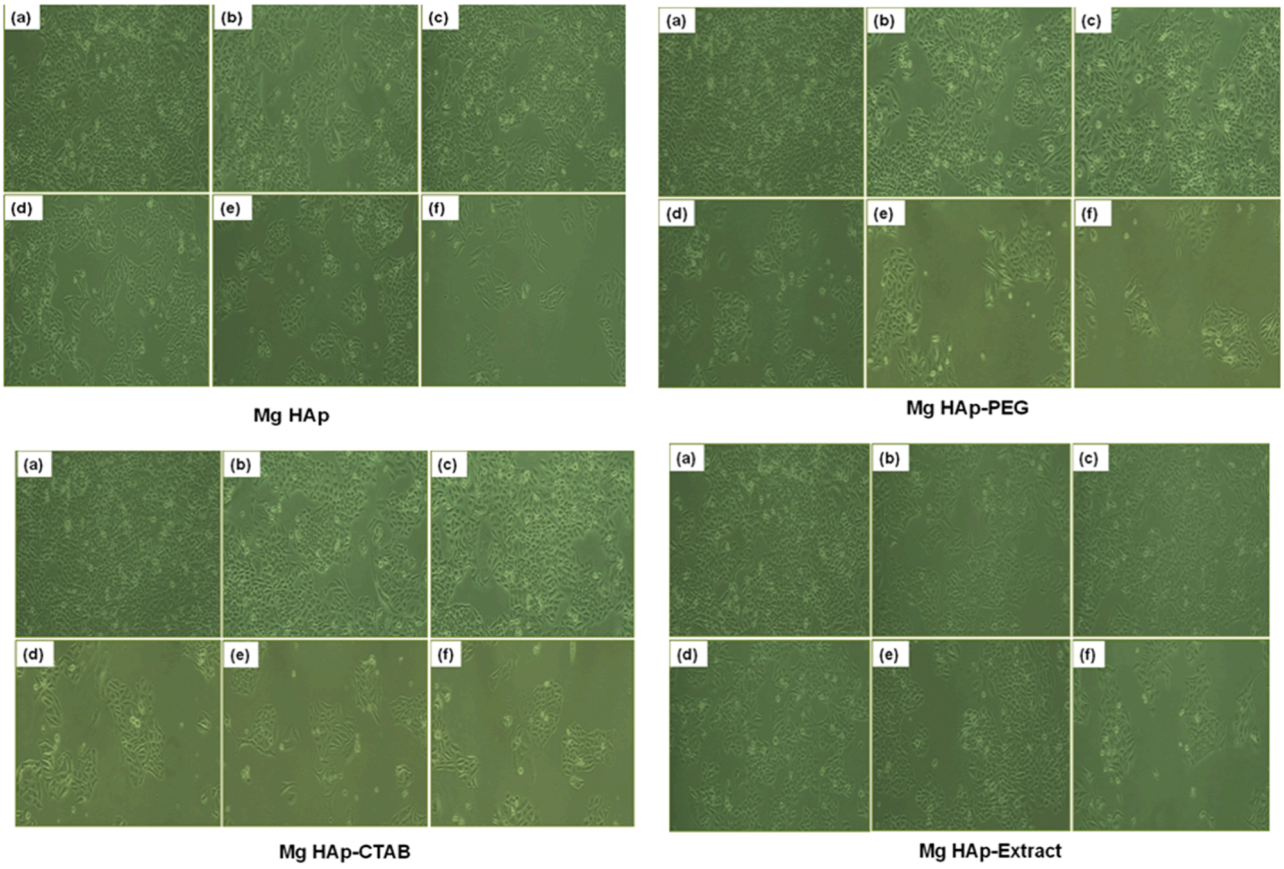

Fig. 16. Anticancerous activity of Mg^{2+} doped HAp NPs calcined at 500 °C, (a) Control, (b) 6.25 μg/ml, (c) 12.5 μg/ml, (d) 25 μg/ml, (e) 50 μg/ml, (f) 100 μg/ml, scale bar: 100 μm.

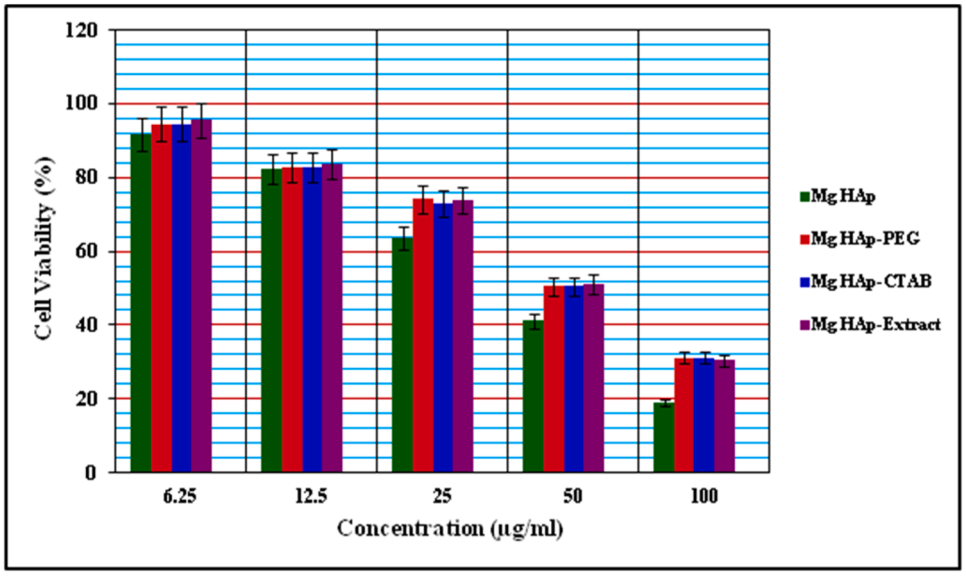

Fig. 17. Anticancerous activity of Mg^{2+} doped HAp NPs calcined at 500 °C, (a) Mg^{2+} HAp, (b) Mg^{2+} HAp-PEG, (c) Mg^{2+} HAp-CTAB and (d) Mg^{2+} HAp- curcumin.

CRediT authorship contribution statement

Saleth Sebastiammal: Conceptualization, Data curation, Formal analysis, Investigation, Methodology, Validation, Visualization, Writing – original draft. **Arul Sigamani Lesly Fathima:** Conceptualization, Data curation, Project administration, Software, Supervision, Validation, Visualization. **Khalid A. Al-Ghanim:** Resources, Software, Validation, Writing – review & editing. **Marcello Nicoletti:** Software, Validation, Writing – review & editing. **Gurunathan Baskar:** Software, Writing – review & editing. **Jayaraj Iyyappan:** Software, Writing – review & editing. **Marimuthu Govindarajan:** Conceptualization, Data curation, Validation, Writing – review & editing.

Declaration of Competing Interest

The authors declare that they have no known competing financial interests or personal relationships that could have appeared to influence the work reported in this paper.

Data availability

Data will be made available on request.

Acknowledgements

The authors express their sincere appreciation to the Researchers Supporting Project Number (RSP2023R48), King Saud University, Riyadh, Saudi Arabia.

References

[1] R. Ahmadi, N. Asadpourchallou, B.K. Kaleji, In vitro study: Evaluation of mechanical behavior, corrosion resistance, antibacterial properties and biocompatibility of HAp/TiO_2/Ag coating on Ti6Al4V/TiO_2 substrate, Surf. Interfaces 24 (2021), 101072, https://doi.org/10.1016/j.surfin.2021.101072.
[2] M. Al-Amin, A.M. Abdul-Rani, M. Rana, S. Hastuty, M. Danish, S. Rubaiee, A. B. Mahfouz, Evaluation of modified 316 L surface properties through HAp suspended EDM process for biomedical application, Surf. Interfaces 28 (2022), 101600, https://doi.org/10.1016/j.surfin.2021.101600.
[3] T. Aswani, V. Pushpa Manjari, B. Babu, S. Muntaz Begum, G. Rama Sundari, K. Ravindranadh, R.V.S.S.N. Ravikumar, Spectral characterizations of undoped and Cu^{2+}doped CdO nanopowder, J. Mol. Struct. 1063 (2014) 178–183, https://doi.org/10.1016/j.molstruc.2014.01.059.
[4] S.P. Bansod, J.K. Parikh, P.K. Sarangi, Pineapple peel waste valorization for extraction of bio-active compounds and protein: Microwave assisted method and Box Behnken design optimization, Environ. Res. 221 (2023), 115237, https://doi.org/10.1016/j.envres.2023.115237.
[5] M. Barjasteh, S.M. Dehnavi, S. Ahmadi Seyedkhani, S.Y. Rahnamaee, M. Golizadeh, Improved biological activities of dual nanofibrous chitosan/bacterial cellulose wound dressing by a novel silver-based metal-organic framework, Surf. Interfaces 36 (2023), 102631, https://doi.org/10.1016/j.surfin.2023.102631.
[6] G. Baskar, A.R. Abinesh, A. Sheik Mohammed Raja, K. Keerthana, A. Supriya, R. Pravin, Green synthesis, characterization and anticancer activity of fungal asparaginase from Aspergillus terreus conjugated on MgO-ZnO nanocomposite against liver cancer cells, Indian J. Exp. Biol. 61 (2023) 761–766, https://doi.org/10.56042/ijeb.v61i10.1642.
[7] S.L. Bee, Y. Bustami, A. Ul-Hamid, Z.A.A. Hamid, Green biosynthesis of hydroxyapatite-silver nanoparticle nanocomposite using aqueous Indian curry leaf (Murraya koengii) extract and its biological properties, Mater. Chem. Phys. 277 (2022), 125455, https://doi.org/10.1016/j.matchemphys.2021.125455.
[8] M.P. Bhat, B. Chakraborty, S.K. Nagaraja, P.V. Gunagambhire, R.S. Kumar, S. Nayaka, A.I. Almansour, K. Perumal, Aspergillus niger CJ6 extract with antimicrobial potential promotes in-vitro cytotoxicity and induced apoptosis against MIA PaCa-2 cell line, Environ. Res. 229 (2023), 116008, https://doi.org/10.1016/j.envres.2023.116008.
[9] E. Boanini, M. Gazzano, A. Bigi, Ionic substitutions in calcium phosphates synthesized at low temperature, Acta Biomater. 6 (2010) 1882–1894, https://doi.org/10.1016/j.actbio.2009.12.041.
[10] C.S. Ciobanu, M.V. Predoi, N. Buton, C. Megier, S.L. Iconaru, D. Predoi, Physicochemical characterization of europium-doped hydroxyapatite thin films with antifungal activity, Coatings 12 (2022) 306, https://doi.org/10.3390/coatings12030306.
[11] B.A. Correa-Piña, O.M. Gomez-Vazquez, S.M. Londoño-Restrepo, L.F. Zubieta-Otero, B.M. Millan-Malo, M.E. Rodriguez-García, Synthesis and characterization of nano-hydroxyapatite added with magnesium obtained by wet chemical precipitation, Prog. Nat. Sci. 31 (2021) 575–582, https://doi.org/10.1016/j.pnsc.2021.06.006.
[12] A.P. Craig, A.S. Franca, J. Irudayaraj, Vibrational spectroscopy for food quality and safety screening. High Throughput Screening For Food Safety Assessment, Elsevier, 2015, pp. 165–194, https://doi.org/10.1016/b978-0-85709-801-6.00007-1.
[13] P. Durairaj, T. T Maruthavanan, S. Manjunathan, S. Saminathan Subashini, S. L. Rokhum, G. Baskar, Microwave assisted synthesis, characterization and bioactivity evaluation of a cobalt (II) complex with a novel Schiff base ligand derived from phenylacetyl urea and salicylaldehyde, J. Mol. Struct. 1295 (2024), 136650, https://doi.org/10.1016/j.molstruc.2023.136650.
[14] C. Garbo, J. Locs, M. D'Este, G. Demazeau, A. Mocanu, C. Roman, O. Horovitz, M. Tomoaia-Cotisel, Advanced mg, Zn, Sr, Si multi-substituted hydroxyapatites for bone regeneration, Int. J. Nanomed. 15 (2020) 1037–1058, https://doi.org/10.2147/IJN.S226630.
[15] A. Ghanbari, A. Bordbar-Khiabani, F. Warchomicka, C. Sommitsch, B. Yarmand, A. Zamanian, PEO/Polymer hybrid coatings on magnesium alloy to improve biodegradation and biocompatibility properties, Surf. Interfaces 36 (2023), 102495, https://doi.org/10.1016/j.surfin.2022.102495.
[16] E. Grela, J. Kozłowska, A. Grabowiecka, Current methodology of MTT assay in bacteria - A review, Acta Histochem. 120 (2018) 303–311, https://doi.org/10.1016/j.acthis.2018.03.007.
[17] Z. Hongquan, Y. Yuhua, W. Youfa, L. Shipu, Morphology and formation mechanism of hydroxyapatite whiskers from moderately acid solution, Mater. Res. 6 (2003) 111–115, https://doi.org/10.1590/s1516-14392003000100020.
[18] N.E. Hsu, W.K. Hung, Y.F. Chen, Origin of defect emission identified by polarized luminescence from aligned ZnO nanorods, J. Appl. Phys. 96 (2004) 4671–4673, https://doi.org/10.1063/1.1787905.
[19] M. Iafisco, A. Ruffini, A. Adamiano, S. Sprio, A. Tampieri, Biomimetic magnesium-carbonate-apatite nanocrystals endowed with strontium ions as anti-osteoporotic trigger, Mater. Sci. Eng. C Mater. Biol. Appl. 35 (2014) 212–219, https://doi.org/10.1016/j.msec.2013.11.009.
[20] N.A. Ibrahim, B.M. Eid, E.M. El-Zairy, E. Emam, S. Barakat, Environmentally sound approach for imparting antibacterial and UV-protection functionalities to linen cellulose using ascorbic acid, Int. J. Biol. Macromol. 135 (2019) 88–96, https://doi.org/10.1016/j.ijbiomac.2019.05.113.
[21] S.L. Iconaru, M.V. Predoi, P. Chapon, S. Gaiaschi, K. Rokosz, S. Raaen, M. Motelica-Heino, D. Predoi, Investigation of spin coating cerium-doped hydroxyapatite thin films with antifungal properties, Coatings 11 (2021) 464, https://doi.org/10.3390/coatings11040464.
[22] R. Ishwarya, B. Vaseeharan, S. Subbaiah, A.K. Nazar, M. Govindarajan, N. S. Alharbi, S. Kadaikunnan, J.M. Khaled, M.N. Al-anbr, Sargassum wightii-synthesized ZnO nanoparticles – from antibacterial and insecticidal activity to immunostimulatory effects on the green tiger shrimp Penaeus semisulcatus, J. Photochem. Photobiol. B Biol. 183 (2018) 318–330, https://doi.org/10.1016/j.jphotobiol.2018.04.049.
[23] A. Iswarya, B. Vaseeharan, M. Anjugam, B. Ashokkumar, M. Govindarajan, N. S. Alharbi, S. Kadaikunnan, J.M. Khaled, G. Benelli, Multipurpose efficacy of ZnO nanoparticles coated by the crustacean immune molecule β-1, 3-glucan binding protein: Toxicity on HepG2 liver cancer cells and bacterial pathogens, Colloids Surf. B 158 (2017) 257–269, https://doi.org/10.1016/j.colsurfb.2017.06.035.
[24] Y. Jiang, K. He, Nanobiotechnological approaches in osteosarcoma therapy: Versatile (nano) platforms for theranostic applications, Environ. Res. 229 (2023), 115939, https://doi.org/10.1016/j.envres.2023.115939.
[25] K. Kala, M.S. Jeyalakshmi, S. Mohandoss, R. Chandrasekaran, Evolution of anticancer, antioxidant and photocatalytic activities of biosynthesized MnO_2 nanoparticles using aqueous extract of Sida acuta, Surf. Interfaces 40 (2023), 103136, https://doi.org/10.1016/j.surfin.2023.103136.
[26] V. Kalaiselvi, R. Mathammal, S. Vijayakumar, B. Vaseeharan, Microwave assisted green synthesis of Hydroxyapatite nanorods using Moringa oleifera flower extract and its antimicrobial applications, Int. J. Vet. Sci. Med. 6 (2018) 286–295, https://doi.org/10.1016/j.ijvsm.2018.08.003.
[27] V. Karthika, P. Kaleeswarran, K. Gopinath, A. Arumugam, M. Govindarajan, N. S. Alharbi, J.M. Khaled, M.N. Al-anbr, G. Benelli, Biocompatible properties of nano-drug carriers using TiO_2-Au embedded on multiwall carbon nanotubes for targeted drug delivery, Mater. Sci. Eng. C 90 (2018) 589–601, https://doi.org/10.1016/j.msec.2018.04.094.
[28] M. Kavitha, R. Subramanian, K.S. Vinoth, R. Narayanan, G. Venkatesh, N. Esakkiraja, Optimization of process parameters for solution combustion synthesis of Strontium substituted Hydroxyapatite nanocrystals using Design of Experiments approach, Powder Technol. 271 (2015) 167–181, https://doi.org/10.1016/j.powtec.2014.10.046.
[29] O. Kaygili, S. Keser, Sol–gel synthesis and characterization of Sr/Mg, Mg/Zn and Sr/Zn co-doped hydroxyapatites, Mater. Lett. 141 (2015) 161–164, https://doi.org/10.1016/j.matlet.2014.11.078.
[30] S. Lara-Ochoa, W. Ortega-Lara, C.E. Guerrero-Beltrán, Hydroxyapatite nanoparticles in drug delivery: Physicochemistry and applications, Pharmaceutics 13 (2021) 1642, https://doi.org/10.3390/pharmaceutics13101642.
[31] W. Li, Y. Lu, K. Liu, W. Wen, M. Liu, H. Li, C. Zhou, B. Luo, Preparation of HAp whiskers with or without Mg ions and their effects on the mechanical properties and osteogenic activity of poly(,-lactide), Compos. B Eng. 196 (2020), 108137, https://doi.org/10.1016/j.compositesb.2020.108137.
[32] Y. Liu, D. Hou, G. Wang, A simple wet chemical synthesis and characterization of hydroxyapatite nanorods, Mater. Chem. Phys. 86 (2004) 69–73, https://doi.org/10.1016/j.matchemphys.2004.02.009.
[33] S.M. Londoño-Restrepo, B.M. Millán-Malo, A. Del Real-López, M.E. Rodriguez-García, In situ study of hydroxyapatite from cattle during a controlled calcination process using HT-XRD, Mater. Sci. Eng. C Mater. Biol. Appl. 105 (2019), 110020, https://doi.org/10.1016/j.msec.2019.110020.
[34] P. Martins da Silva Filho, P. Higor Rocha Mariano, A. Lopes Andrade, J. Barros Arrais Cruz Lopes, A. de Azevedo Pinheiro, M. Itala Geronimo de Azevedo, S. Carneiro de Medeiros, M. Alves de Vasconcelos, S. Gonçalvez da Cruz Fonseca, T. Barbosa Grangeiro, L. Gonzaga de França Lopes, E. Henrique Silva Sousa, E. Holanda Teixeira, E. Longhinotti, Antibacterial and antifungal action of CTAB-containing silica nanoparticles against human pathogens, Int. J. Pharm. 641 (2023), 123074, https://doi.org/10.1016/j.ijpharm.2023.123074.
[35] V.K. Mishra, S.B. Rai, B.P. Asthana, O. Parkash, D. Kumar, Effect of annealing on nanoparticles of hydroxyapatite synthesized via microwave irradiation: Structural and spectroscopic studies, Ceram. Int. 40 (2014) 11319–11328, https://doi.org/10.1016/j.ceramint.2014.03.128.
[36] F. Moghaddasi, M.R. Housaindokht, M. Darroudi, M.R. Bozorgmehr, A. Sadeghi, Synthesis of nano curcumin using black pepper oil by O/W Nanoemulsion

Technique and investigation of their biological activities, Lebenson. Wiss. Technol. 92 (2018) 92–100, https://doi.org/10.1016/j.lwt.2018.02.023.
[37] T. Nagyné-Kovács, L. Studnicka, A. Kincses, G. Spengler, M. Molnár, M. Tolner, I. E. Lukács, I.M. Szilágyi, G. Pokol, Synthesis and characterization of Sr and Mg-doped hydroxyapatite by a simple precipitation method, Ceram. Int. 44 (2018) 22976–22982, https://doi.org/10.1016/j.ceramint.2018.09.096.
[38] R. Nallendran, G. Selvan, A.R. Balu, NiO coupled CdO nanoparticles with enhanced magnetic and antifungal properties, Surf. Interfaces 15 (2019) 11–18, https://doi.org/10.1016/j.surfin.2019.02.002.
[39] D. Nath, F. Singh, R. Das, X-ray diffraction analysis by Williamson-Hall, Halder-Wagner and size-strain plot methods of CdSe nanoparticles- a comparative study, Mater. Chem. Phys. 239 (2020), 122021, https://doi.org/10.1016/j.matchemphys.2019.122021.
[40] V. Nguyen, V. Vu, The Nguyen, T. Nguyen, V. Tran, P. Nguyen-Tri, Antibacterial activity of TiO_2- and ZnO-decorated with silver nanoparticles, J. Compos. Sci. 3 (2019) 61, https://doi.org/10.3390/jcs3020061.
[41] E. Paliersе, C. Hélary, J.M. Krafft, I. Génois, S. Masse, G. Laurent, M.I. Alvarez Echazu, M. Selmane, S. Casale, L. Valentin, A. Miche, B.C.L. Chan, C.B.S. Lau, M. Ip, M.F. Desimone, T. Coradin, C. Jolivalt, Baicalein-modified hydroxyapatite nanoparticles and coatings with antibacterial and antioxidant properties, Mater. Sci. Eng. C Mater. Biol. Appl. 118 (2021), 111537, https://doi.org/10.1016/j.msec.2020.111537.
[42] S.S. Park, U. Farwa, I. Park, B.G. Moon, S.B. Im, B.T. Lee, In-vivo bone remodeling potential of Sr-d-Ca-P /PLLA-HAp coated biodegradable ZK60 alloy bone plate, Mater. Today Bio 18 (2023), 100533, https://doi.org/10.1016/j.mtbio.2022.100533.
[43] A. Rajiv, A. Kapse, V.K. Singh, M.S. Chauhan, A. Awasthi, P. Singh, Chitosan-modified magnesium oxide hybrid nanomaterial: A dual approach for bacterial and cancer cell eradication, Surf. Interfaces 44 (2024), 103628, https://doi.org/10.1016/j.surfin.2023.103628.
[44] J. Ren, H. Wu, Z. Lu, Q. Qin, X. Jiao, G. Meng, W. Liu, G. Li, pH-driven preparation of pea protein isolate-curcumin nanoparticles effectively enhances antitumor activity, Int. J. Biol. Macromol. 256 (2024), 128383, https://doi.org/10.1016/j.ijbiomac.2023.128383.
[45] M. Rostami, A. Badiei, A.M. Sorouri, M. Fasihi-Ramandi, M.R. Ganjali, M. Rahimi-Nasrabadi, F. Ahmadi, Cur-loaded magnetic $ZnFe_2O_4$@L-cysteine – Ox, N-rich mesoporous -gC3N4 nanocarriers as a targeted sonodynamic chemotherapeutic agent for enhanced tumor eradication, Surf. Interfaces 30 (2022), 101900, https://doi.org/10.1016/j.surfin.2022.101900.
[46] S. Sebastiammal, A.S. Lesly Fathima, S. Alarifi, S. Mahboob, J. Henry, M. R. Kavipriya, M. Govindarajan, M. Nicoletti, B. Vaseeharan, Synthesis and physicochemical characteristics of Ag-doped hydroxyapatite nanoparticles, and their potential biomedical applications, Environ. Res. 210 (2022), 112979, https://doi.org/10.1016/j.envres.2022.112979.
[47] M. Shokri, M. Kharaziha, H.A. Tafti, M.B. Eslaminejad, R.M. Aghdam, Synergic role of zinc and gallium doping in hydroxyapatite nanoparticles to improve osteogenesis and antibacterial activity, Biomater. Adv. 134 (2022), 112684, https://doi.org/10.1016/j.msec.2022.112684.
[48] Y. Sihn, H.M. Yang, C.W. Park, I.H. Yoon, I. Kim, Post-substitution of magnesium at CaI of nano-hydroxyapatite surface for highly efficient and selective removal of radioactive 90Sr from groundwater, Chemosphere 295 (2022), 133874, https://doi.org/10.1016/j.chemosphere.2022.133874.
[49] R. Subramanian, P. Murugan, G. Chinnadurai, K. Ponmurugan, N.A. Al-Dhabi, Experimental studies on caffeine mediated synthesis of hydroxyapatite nanorods and their characterization, Mater. Res. Express 7 (2020), 015022, https://doi.org/10.1088/2053-1591/ab619a.
[50] Terauchi, M., Takahashi, H., Handa, N., Murano, T., Koike, M., Kawachi, T., Imazono, T., Koeda, M., Nagano, T., Sasai, H., Oue, Y., Yonezawa, Z., Kuramoto, S., 2012. A new WDS spectrometer for valence electron spectroscopy based on electron microscopy [WWW Document]. URL http://101.201.233.138:8100/admin/static/uploadfiles/20170419/008a9e48-fa8f-4ccd-b3cf-af45f1ddfa8e.pdf (accessed 5.18.23).
[51] S. Umavathi, S. Mahboob, M. Govindarajan, K.A. Al-Ghanim, Z. Ahmed, P. Virik, N. Al-Mulhm, M. Subash, K. Gopinath, C. Kavitha, Green synthesis of ZnO nanoparticles for antimicrobial and vegetative growth applications: A novel approach for advancing efficient high quality health care to human wellbeing, Saudi J. Biol. Sci. 28 (2021) 1808–1815, https://doi.org/10.1016/j.sjbs.2020.12.025.
[52] S.C. Veerla, D.R. Kim, J. Kim, H. Sohn, S.Y. Yang, Controlled nanoparticle synthesis of Ag/Fe co-doped hydroxyapatite system for cancer cell treatment, Mater. Sci. Eng. C Mater. Biol. Appl. 98 (2019) 311–323, https://doi.org/10.1016/j.msec.2018.12.148.
[53] E. Yousif, A. Majeed, K.W. Al-Sammarrae, N. Salih, J. Salimon, B.M. Abdullah, Metal complexes of Schiff base: Preparation, characterization and antibacterial activity, Arab. J. Chem. 10 (2017) S1639–S1644, https://doi.org/10.1016/j.arabjc.2013.06.006.